ChemComm

HIGHLIGHT

View Article Online
View Journal | View Issue

Check for updates

Cite this: *Chem. Commun.*, 2025, 61, 3777

The nucleation and growth mechanism of spherical Li for advanced Li metal anodes – a review†

Mengting Wang,‡[a] Xingtong Guo,‡[a] Rui Luo,[a] Xiaonuo Jiang,[a] Yongfu Tang *[b] and Tao Wei *[a]

Received 25th December 2024,
Accepted 29th January 2025

DOI: 10.1039/d4cc06729k

rsc.li/chemcomm

Metallic lithium (Li) is known as the "Holy Grail" of anode materials in the research area of Li-based batteries. However, Li metal anodes (LMAs) are plagued by infinite volume changes and dendrite formation during operation. Spherical Li exhibits rounded surfaces, which effectively mitigates the short circuit risks associated with dendritic Li, and has the smallest specific surface area compared to other deposit morphologies, thus enabling less electrolyte consumption and higher Coulombic efficiency (CE). What's more, three-dimensional (3D) conductive frameworks have good mechanical robustness and flexibility to withstand the volume changes that occur during cycling. This review systematically depicts the theoretical models for Li deposition, the mechanisms and formation conditions of spherical Li, and the benefits of the Li deposition model as well as the advantages of combining Li spheres with 3D conductive frameworks based on our previous works. We hope that this review can inspire researchers in this filed to pave the way for advanced LMAs.

Published on 30 mis Genver 2025. Downloaded on 19/04/2026 22:10:03.

1. Introduction

The escalating consumption of fossil fuels and global environmental degradation problems are propelling the surging demand for renewable, eco-friendly, and cost-effective energy conversion or storage technologies.[1–4] Among different kinds of new energy technologies, batteries have achieved significant success due to their user-friendly nature and cost-effectiveness.[5–7] After the invention of the first battery by Volta in the 19th century, a variety of electrochemical batteries have gradually stepped into the commercial market, including lead–acid, nickel–cadmium, and lithium-ion batteries (LIBs).[8–10] Among them, the LIB with Li cobaltate as the positive electrode and carbon material as the negative electrode, which was successfully launched by Sony Corporation of Japan in 1991, occupies an important position in the commercial market; this kind of battery overcomes the memory effect of the traditional batteries, and has the advantages of high energy density and long cycle life, and hence is rapidly occupying the consumer electronics market.[11–16] At the beginning of the 21st century, LIBs continued to expand in the field of consumer electronics, revolutionising the way modern life is communicated and transported, enabling the rise of camcorders, mobile phones, laptop computers and more recently electric vehicles. However, the current graphite anode (370 mA h g^{-1}) is not suitable for powering the booming development of new and advanced electronics.[17–20] Fortunately, owing to the remarkable theoretical capacity of Li metal (3860 mA h g^{-1}) and the exceptionally low electrochemical potential (−3.04 V *vs.* H^+/H_2), the early lapsed Li-metal batteries (LMBs) have returned to the public eyes.[21–24] This is also an opportune moment to reassess the two primary challenges inherent in LMBs.

(1) The Li dendrite problem

The disordered characteristics due to the uneven deposition of Li will trigger dendritic Li growth, cause repeated elongation, and even puncture the separator so that the batteries short-circuit, resulting in safety accidents.[25–29]

(2) The infinite volume expansion problem

Continuous relative volume expansion will make the solid electrolyte interface (SEI) film fracture, exposing the surface of fresh Li in contact with the electrolyte, resulting in endless consumption of the electrolyte and Li, reducing the Coulombic efficiency (CE) and producing "dead Li".[30–35]

LMBs are plagued by these two major issues, which have hindered their commercial success. Consequently, strategies aimed at inhibiting dendrite growth and moderating volume changes have sparked intense discussions over the past two

[a] School of Energy and Power, Jiangsu University of Science and Technology, Zhenjiang 212003, China. E-mail: wt863@126.com
[b] State Key Laboratory of Metastable Materials Science and Technology (MMST), Hebei Key Laboratory of Applied Chemistry, Yanshan University, Qinhuangdao 066004, P. R. China. E-mail: tangyongfu@ysu.edu.cn

† Electronic supplementary information (ESI) available. see DOI: https://doi.org/10.1039/d4cc06729k

‡ These authors contributed equally to this work.

Published on 30 mis Genver 2025. Downloaded on 19/04/2026 22:10:03.

decades. These solutions primarily focus on the implementation of Li alloy electrodes to mitigate dendrite formation,[36–39] the improvement of organic electrolytes and the establishment of artificial passivation films for stabilizing the interface of Li metal/electrolyte,[40–43] the realization of solid-state electrolytes to improve shear modulus and safety,[44–47] and developing a structured anode design by taking advantage of the revolution in nanotechnology and nanomaterials.[48–51]

The development of LMBs has been propelled by these proposed strategies; however the behavior of Li deposition is one of the most critical issues which is still waiting to be explored. In general terms, Li metal deposits exhibit various shapes, such as mossy,[52,53] fibrous,[54,55] whisker-like,[56] planar nodular,[2,57] and spherical forms.[57,58] Randomly distributed and disorganized Li deposits with needle-like or branching morphology can give rise to significant safety concerns, whereas ordered and uniform Li deposits with smooth surfaces pose challenges in terms of separator penetration.[52,59] Furthermore, among the various depositional morphologies, spherical Li metal deposits exhibit rounded surfaces and a lack of protruding tips, effectively mitigating the short circuit risks associated with dendritic Li deposits while also contributing to volume change mitigation.[60] Additionally, spherical Li has the smallest specific surface area compared to other deposit situations, which reduces the contact area between the Li anode and the electrolyte, resulting in better electrochemical performance, such as higher CE and longer cycling life.[61] Considering the aforementioned factors, spherical Li deposition holds immense potential for advancing highly energy-efficient Li metal anodes (LMAs). Currently, numerous studies have documented the emergence of spherical Li deposits with promising results.[62–64] However, there remains a notable gap in comprehensive and systematic elucidation regarding the formation mechanisms and influencing conditions of these spherical Li deposits. Consequently, this work is aiming to deliver a systematic overview of spherical Li deposition to facilitate advancements in the field and inspire future innovations in LMA design.

In this study, firstly, some theoretical models that have been developed to interpret the mathematical relationships between different Li metal structures and their main influencing issues are summarized. Secondly, the distinctive properties and electrochemical behavior of polycrystalline Li are comprehensively elucidated, thereby facilitating the development of targeted inhibition strategies. Subsequently, a summarized description of the formation advantages, formation conditions, and formation mechanisms of spherical Li deposits is given. Finally, the benefits of the Li deposition model are analyzed and the advantages of combining Li spheres with three-dimensional (3D) conductive frameworks are considered based on our previous works.

2. General mechanism and growth morphology of Li

Li stands out among the alkali metals due to its distinct properties, such as being the lightest and having the smallest atomic diameter. These intrinsic features endow Li with a remarkable high capacity and enable rapid transfer.[61] Therefore, the investigation of using Li metal as the anode for applications has been a hot research topic. Nevertheless, there are still many challenges for the wide commercialization of LMAs. The high reactivity and low potential of Li metal make Li unstable when it encounters electrolytes in rechargeable batteries, resulting in a potential crisis. In brief, upon contact with the electrolyte, Li undergoes corrosion and experiences a decrease in its utilization. Simultaneously, during the electrodeposition of Li, Li^+ lacks a definitive position and exhibits non-homogeneous initial nucleation of Li.[65] It is widely recognized that the formation of dendritic Li significantly hinders the advancement of LMBs. The prevention of Li dendrite growth has been a major focus and challenge in this area. Despite the emergence of numerous strategies to inhibit dendrite growth, there is a lack of comprehensive exploration into Li deposition behavior, which directly influences dendrite formation. Therefore, this summary will briefly introduce the Li deposition behavior from the perspectives of multi-physical fields (ion concentration field model, electric field model) and Li nucleation. It aims to reveal the formation mechanism of different Li morphologies and make contributions to correctly guiding the smooth plating of Li.

2.1. Modeling Li deposition behavior with multifield and nucleation models

The Li deposition process follows the basic electrochemical principles, including four steps: (1) ion diffusion, (2) ion adsorption, (3) ion reduction nucleation, and (4) Li metal growth. According to the simplified electrodeposition behavior, solvated Li^+ migrates to the anode side as a result of electric fields, adsorbs on the surface of the electrode through the double electric layer effect, undergoes the desolvation process, and finally produces Li metal on the anode through continuous reduction reactions. Among them, nucleation is widely acknowledged as a pivotal process in dictating the final form of deposited Li and ensuring anode surface stability during subsequent plating/stripping cycles. The Li^+ diffusion and adsorption process as a precursor strictly controls Li nucleation behavior and provides balanced "power" and "escort" for Li nucleation.[66,67] Consequently, when LMBs are operated under practical conditions – such as electrolyte limitations and elevated operating current densities – the ion adsorption and diffusion processes exert a more pronounced influence on Li deposition compared to the nucleation and growth phases.[63] Under these circumstances, parameters including current distribution, Li-ion homogeneity, and salt concentration at the interface of the anode side critically determine the final morphologies and cycle stability of the LMA.[68,69] Therefore, a better understanding of the close connection between the ion concentration field and the electric field distribution and the morphological evolution of Li is needed to develop precise strategies to regulate diffusion and adsorption.

(1) The well-known Sand's time (τ_{Sand}) model is based on the ion concentration field. In 1901, Sand *et al.*[70] discovered the formation of branching structures in the electrodeposition process of a mixture of $CuSO_4$ and H_2SO_4, which was controlled by the salt concentration close to the electrode surface. In the process of deposition, positively charged ions and negatively

 This journal is © The Royal Society of Chemistry 2025

Published on 30 mis Genver 2025. Downloaded on 19/04/2026 22:10:03.

charged ions move in opposite directions. Cations gather close to the anode, while negatively charged ions go opposite to the cathode side. Concurrently, positively charged ions are used up during the process of depositing the metal, resulting in a gradual reduction of the amount of salt on the surface of the positive electrode. When the salt concentration on the anode surface becomes 0, the stable deposition will change to a self-amplifying dendritic growth mode. The onset of dendrite growth is represented by τ_{Sand} (eqn (1)):

$$\tau = \pi D\left(\frac{C_0 e Z_c}{2J}\right)^2\left(\frac{\mu_a + \mu_c}{\mu_a}\right)^2 \quad (1)$$

Here, D represents the binary diffusion coefficient, e denotes the elementary charge, C_0 stands for the initial concentration of cations (Li salt), J signifies the effective current density, Z_c indicates the cation charge number, and μ_c and μ_a represent the migration numbers of cations and anions respectively. Sand's model provides a quantitative understanding of the development of Li dendrites. It suggests that by reducing the effective current density or increasing the speed of ion movement, the lifespan of τ_{Sand} could be prolonged. Furthermore, in 1999, Brissot *et al.*[71] proposed the utilization of a bipolar diffusion equation at the electrode for the detection of changes in ion concentration, as represented by eqn (2):

$$\frac{\partial C}{\partial x}(x) = \frac{J\mu_a}{eD(\mu_a + \mu_c)} \quad (2)$$

The symbolic meaning here is equivalent to the equation (eqn (1)) above. If $d_c/d_x < 2C_0/L$ (where L is the inner electrode distance), the concentration of the ion at the negative electrode remains stable, and both the electrostatic potential value and the concentration gradient remain unchanged, indicating uniform Li^+ deposition. However, when $d_c/d_x < 2C_0/L$, as depicted in Fig. 1(a), the ion concentration at the electrode drops to 0, and there is a spike in the potential value. The critical diffusion time derived at the inflection point corresponds to the Sand time. In addition, to simplify the identification of crucial running conditions for the Li negative electrode in actual scenarios, by utilizing the inverse correlation between dendrite nucleation time and total deposition capacity, τ_{Sand} is changed into Sand's capacity ($C_{Sand} = J\tau_{Sand}$).[52]

While Sand's time model holds certain reference value for predicting battery performance, its accuracy is limited by multiple factors. The intricate internal microstructure of batteries, exemplified by the irregular size and distribution of electrode material particles, results in variations in ion diffusion paths and velocities, thereby impacting model predictions. Moreover, environmental factors such as temperature fluctuations significantly influence chemical reaction rates and ionic conductivity. Particularly at low temperatures, the actual discharge duration of batteries markedly deviates from model predictions. Additionally, polarization during high-rate charging and discharging further contributes to discrepancies in capacity and timing. Considering these existing limitations, by setting some specific conditions, Sand's time model can still provide more accurate prediction results. When the battery operates in a relatively

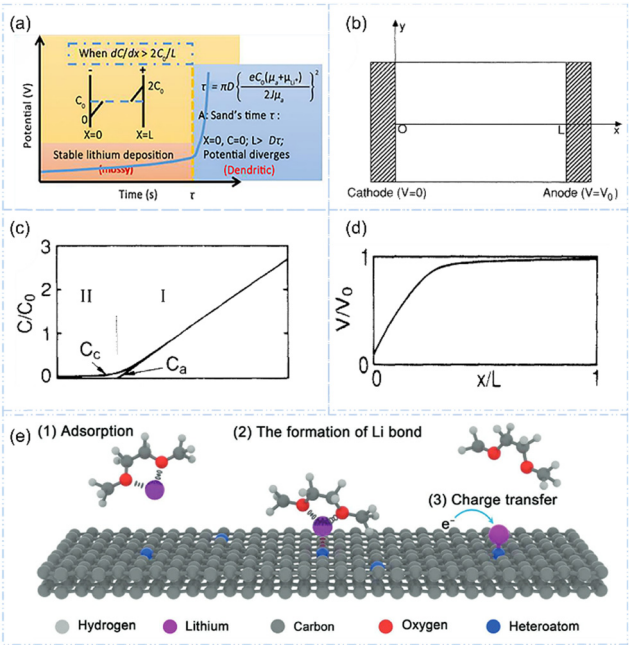

Fig. 1 (a) At $J > J_{limit}$ (semi-infinite approximation), the ionic concentration drops to zero and the cell potential diverges at Sand's time.[71] (b) Illustration of the simulation-based symmetrical cell setup. (c) The distribution of cation/anion concentration. (d) The voltage distribution along the battery.[72] (e) Illustration of the nucleation processes of Li on conductive carbon frameworks.[73]

stable ambient temperature environment with low charge/discharge multipliers, the chemical reactions within the battery are closer to the ideal state assumed by the model. At this time, the ion diffusion rate is relatively stable, the polarization phenomenon is not obvious, and the microscopic difference of electrode materials has a relatively small impact on the overall performance, so Sand's time model can predict the charging and discharging time of the battery more accurately.[74]

(2) The space charge theory is a conceptual framework that relies on the presence of an electric field. The space charge theory which was first introduced by Chazalviel *et al.* in 1990[75] seeks to explain the formation of dendrites in terms of the unequal migration of positively and negatively charged particles. This model is suitable for situations involving weak electrolytes, where the movement of ions is only influenced by their mobility and diffusion coefficient and not by the convection of the electrolyte.[76] It highlights the significance of anions in the process of charging. Specifically, during rapid Li plating, while Li^+ can be continuously replenished, anions cannot; thus, they are more significantly influenced by the electric field in terms of concentration. As a result, depletion zones form quickly at the Li surface during the process of charging, causing a reduction in potential. With the preferential depletion of anions, the accelerated movement of cations is also rapidly depleted at the interface, causing the priority deposition of new cations at the discharge tip. A concentrated space charge and a strong electric field will form due to the depletion of anions and accumulation of Li close to the anode, which promotes dendrite

Published on 30 mis Genver 2025. Downloaded on 19/04/2026 22:10:03.

growth. It is noteworthy that ion concentration and electrostatic potential are also calculated by Chazalviel *et al.* in thin rectangular symmetric cells to validate this model.[72] As can be seen in Fig. 1(b–d), region I represents the bulk electrolyte, while region II corresponds to the small domain (space charge) on and around the surface of the electrode. When the supply rate of Li^+ (Li^+ mobility) in the ion concentration distribution diagram shown in Fig. 1(c) is lower than the consumption rate of Li^+ (reaction rate), dendrite growth will be initiated. Simultaneously, in the voltage curve distribution diagram shown in Fig. 1(d), a space charge region still exists, generating a significant local electric field and inducing dendrite formation.

Similarly, the prediction of the space charge model in real battery systems can be affected by a number of factors. Space charge models typically rely on simplifying assumptions, such as the assumption of a homogeneous and ideal electrode/electrolyte interface. However, real battery interfaces exhibit microscopic roughness, impurities, and crystal defects, making it challenging to accurately characterize these complex interfacial properties. Furthermore, space charge models often concentrate solely on charge-related factors, neglecting the intricate effects of multi-physical field interactions, including thermal effects, stress–strain, and material diffusion. However, when the battery is in a relatively stable state of low-rate charge and discharge, the temperature inside the battery changes little, the multi-physical field coupling effect is relatively weak, and the electrode/electrolyte interface changes slowly. In this case, the space charge model based on the theory of static charge distribution and simple electric field hypothesis can better describe the charge transfer and ion transport process inside the battery. The prediction of the open circuit voltage and the ion concentration distribution in equilibrium state has high accuracy.

The relationship between the formation of dendrites and the controlled salt consumption on the electrode surface has been established in the aforementioned models, and the estimated critical growth conditions of dendrites were relatively consistent. Therefore, in order to control early Li plating behavior, it is essential to consider the mobility of cations and anions, as well as the initial concentration of electrolytes, salts, and current density.[59,77–79] The following reduction of Li^+ to metallic Li participates the nucleation and growth of crystals, and it is vital that the nucleation site plays here in the Li deposition process, it will further affect the final deposition morphology greatly.[80,81] Currently, several nucleation models are described in the literature to explore the behavior of Li deposition, which are summarized below.

(1) The heterogeneous nucleation of Li. This model refers to the deposition of Li metal on the collector surface, where Li^+ gains electrons and initiates plating. In this case, the final Li deposition pattern is determined by the initial nucleation morphology. Therefore, it is necessary to interpret and control heterogeneous mutually reinforcing nuclei carefully and fully.

Ely *et al.*[82] conducted a study on heterogeneous nucleation using mathematical simulation. Five distinct states of heterogeneous nucleation and growth were classified: nucleation suppression, long incubation time, short incubation time, early growth and late growth. Thermodynamically unstable nucleating embryos have a tendency to dissolve into electrolytes when they are in a condition of nucleation inhibition. Afterward, the embryos experienced coarsening due to Gibbs–Thomson interaction during an extended incubation period. Beyond the critical overpotential, the reduced incubation time plays a role in creating a more limited range of embryo sizes. Ultimately, Li initiates nucleation at a critical kinetic radius and experiences rapid growth as the overpotential increases. In conclusion, the inhibition of dendrite formation can be achieved through the reduction of surface roughness on the fluid collector, designing smaller particle size of the anode which is below the critical radius, ensuring that the coating overpotential is smaller than the critical value, and optimizing Li deposit infiltration. As depicted in Fig. 1(e), Chen *et al.*[70] drew inspiration from this model and utilized heteroatom-doped carbon to enhance the Li affinity of the collector fluid, thereby achieving a relatively stable nucleation state.

(2) The homogeneous nucleation model. In essence, homogeneous nucleation of Li refers to the process of nucleation occurring between identical substances (*i.e.*, Li and Li). This phenomenon typically involves a subsequent deposition process on the current collector's surface following the initial deposition of Li, potentially influencing the morphological growth of the deposit. Further elaboration on this will be provided in Section 3. Additionally, significant effects are often achieved through the utilization of heterogeneous nucleation models for the modification of metal Li anodes.[83,84] Therefore, further details on this topic will not be expounded upon here.

2.2. Classification and electrochemical behavior of Li crystals

In practical applications, the plating of Li atoms often shows an irregular porous pattern, which can be broadly classified as dendritic Li, whisker-like Li, mossy Li, and smooth Li.[85] Among these structures, smooth Li represents the desired morphology for efficient Li metal plating. However, the most commonly observed irregular deposition structures are whisker-like Li, mossy Li, and dendritic Li. This concise summary aims to discuss and compare the morphology as well as electrochemical behavior of these three distinct forms of Li deposits.

(1) Whisker-like Li. Short circuits in LMBs are caused by whisker-like Li, sometimes referred to as acicular Li, which grows simultaneously along the transverse and longitudinal axes and grows significantly quicker in length than in transverse diameter (Fig. 2(a1 and a2)).[86] In addition, whisker-like Li is typically formed under specific temperature, pressure, and electrochemical conditions, wherein Li^+ preferentially grows along certain crystallographic orientations through a crystal growth mechanism. For instance, at low temperatures, low current densities, and in electrolytes with particular compositions, the formation of whisker-like Li is more likely to be induced. As illustrated in Fig. 2(a3), the formation of Li whiskers in constant-current Li||Li symmetric cells at low currents is often characterized by a slight increase in cell potential.[87] Notably, due to their single-crystal structure and specific growth orientation, Li whiskers exhibit enhanced electronic and ionic conductivity along their length,

 This journal is © The Royal Society of Chemistry 2025

Published on 30 mis Genver 2025. Downloaded on 19/04/2026 22:10:03.

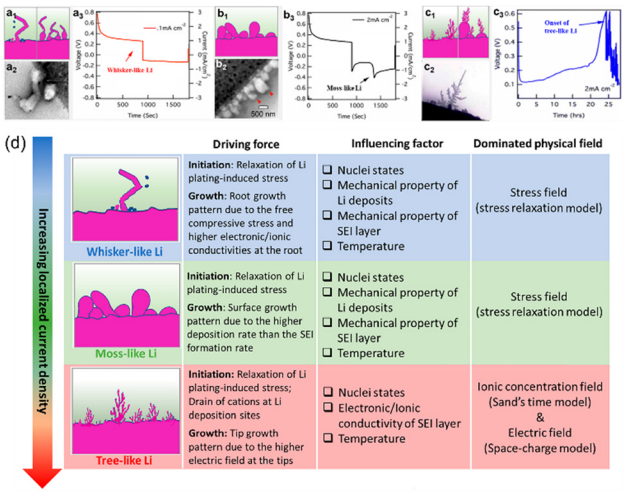

Fig. 2 Comparison of different morphologies leaded by different pathways of Li.[88]

which can improve the battery's charging and discharging efficiency. However, during growth, Li whiskers may penetrate the separator, leading to internal short circuits and adversely affecting the battery's cycle stability.

(2) **Mossy Li.** Mossy Li exhibits a moss-like morphology characterized by the aggregation of numerous minute Li particles, forming a porous and fluffy structure with an irregular surface featuring numerous tiny protrusions and pores, resulting in an overall loose configuration (Fig. 2(b1 and b2)). The formation of mossy Li typically occurs during the charge–discharge cycles of lithium-ion batteries, driven by the combined effects of electrode surface roughness, electrolyte wettability, and Li^+ diffusion rates. These factors lead to non-uniform deposition and aggregation of Li^+ on the electrode surface, resulting in the development of mossy porous structures. Such structures possess a high specific surface area, providing abundant Li^+ storage sites that can enhance the battery's specific capacity. However, due to its porous nature, mossy Li is prone to electrolyte retention, which extends the Li^+ diffusion path during charge–discharge processes, thereby increasing battery polarization and reducing charge–discharge efficiency (Fig. 2(b3)).[89,90] Moreover, due to its loose structure, mossy Li may dislodge during battery operation, leading to potential internal short circuits caused by detached Li particles.

(3) **Dendritic Li.** Dendritic Li, the most prevalent form of Li deposited during electrodeposition, exhibits a fractal structure akin to tree branches, characterized by a main trunk and numerous offshoots that display a complex three-dimensional morphology. These branches extend in multiple directions from the main trunk, resulting in an overall irregular shape that may intertwine during growth (Fig. 2(c1 and c2)). This dendritic morphology primarily forms during the battery charging process due to non-uniform Li^+ deposition on the electrode surface. Factors such as excessively high local current density, rapid Li^+ supply, or impurities in the electrolyte can lead to preferential deposition at specific sites, promoting continuous growth into a dendritic structure. While this structure possesses a large specific surface area, enhancing the contact area between the electrode and the electrolyte and potentially improving battery charge–discharge reaction activity, it is also susceptible to fracture during cycling, leading to the formation of dead Li and subsequent battery capacity loss. As a result, in the constant current symmetric battery test, the dendritic Li later appears as an abnormal voltage curve (Fig. 2(c3)).[65,91,92]

Apart from their distinctions, under specific circumstances, the morphologies of these Li coatings can also interchange.[75] For instance, the dendritic Li deposit will progressively take on the characteristics of moss if the electric field changes and the mean dendritic spacing varies.[52,93] The mossy Li that was initially growing at the root will transform into acicular Li growing at the tip if electrolyte diffusion is restricted.[71,94] As a result, it is challenging to distinguish these three modes because they always coexist in Li deposits. For the purpose of efficiently tailoring electrode surface topography and constructing safe batteries with dendritic-free deposits, it is necessary to simplify the shape of Li deposits readily.

3. Spherical Li

Although the metallic Li is regarded as the ultimate anode for the future advanced Li batteries, low CE and dendritic Li deposition pose serious risks to public safety since there will inevitably be a Li deposition issue due to the ongoing interconversion between Li ions and Li atoms throughout the process of Li plating. As a result, controlling Li deposition is a common strategy used to prevent dendritic development. The emergence of spherical Li deposits in recent years may inhibit the establishment of Li dendrites effectively.

3.1. Advantages of spherical Li

With the study of the mechanism of Li nucleation and growth as well as the morphology and internal structure of Li deposits, spherical Li has attracted more and more attention. Compared with existing Li metal deposits, spherical Li deposits have two important advantages due to their unique morphology. Firstly, spherical Li exhibits distinct morphological characteristics with a smooth surface and the absence of sharp protrusions, thereby effectively mitigating the severe safety risks associated with dendritic Li deposition.[95] Back in 2017, Ye *et al.*[96] capitalized on these spherical attributes to achieve stable electrochemical behavior (Fig. 3(a)). Initially, spherical carbon particles were prepared *via* chemical vapor deposition (CVD) onto a 3D nickel skeleton, followed by gradual coating of these particles with Li growth. Although the direct formation of Li spheres was not achieved in this study, the intermittent coating of spherical carbon particles by Li resulted in an electrode that demonstrated remarkable inhibition of dendrites and high utilization efficiency for Li (Fig. 3(b)), which can be attributed to the unique morphology. At this time, spherical Li deposits had not received widespread attention. More notably, in 2019, Li *et al.*[97] successfully induced the formation of spherical Li deposits by constructing an artificially rich inorganic SEI film which was obtained by using

Published on 30 mis Genver 2025. Downloaded on 19/04/2026 22:10:03.

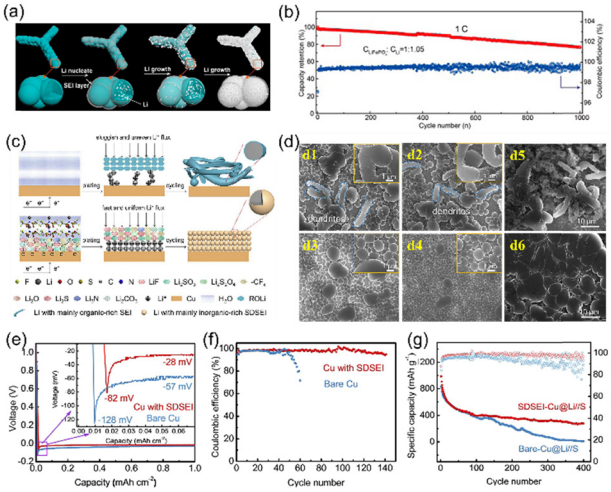

Fig. 3 (a) Illustration of the deposition of Li. (b) Long-term performance of the full cell.[96] (c) Illustrations of the Li deposition behavior on two substrates. (d) SEM images of the 1st Li nuclei on a Cu substrate without or with a salt-derived SEI (donated as SDSEI) film at different areal capacities. (e) Comparison of different substrates at 0.5 mA cm^{-2} after the 1st Li nucleation. (f) CE at 0.5 mA cm^{-2} for Li deposited on a bare Cu substrate and on the Cu substrate with the SDSEI film. (g) Electrochemical performance of different batteries.[97]

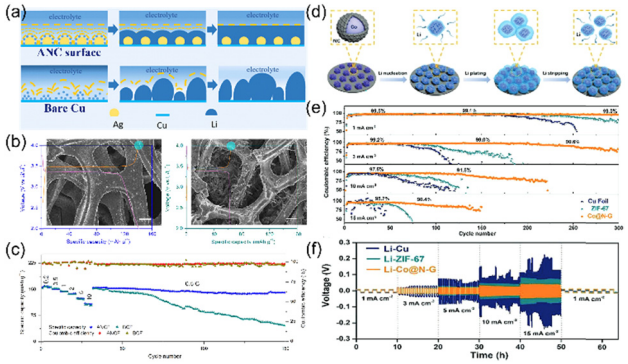

Fig. 4 (a) Deposition of Li on the surface of Cu with Ag nanoparticle coating (named ANC) and bare Cu. (b) Comparison of Li-ANCF and Li-BCF electrodes after 120 cycles. (c) Rate performances of two kinds of batteries.[98] (d) Schematic illustrations of the Li deposition process on Co@N-G. (e) CE of different electrodes with an areal capacity of 1 mA h cm^{-2} at various current densities. (f) Rate performance of various symmetrical cells.[99]

reducing salt anions on a Cu substrate through electroreduction treatment in LiTFSI's water-salt electrolyte (Fig. 3(c)). In the first nuclear topography of Li on different substrates (with and without SEI films), dendritic growth was found on a Cu substrate without SEI films under the current densities of 1 and 2 mA cm^{-2} (Fig. 3(d1 and d2)). However, more uniform growth of Li balls was achieved on Cu substrates pretreated with electroreduction (Fig. 3(d3 and d4)). More pronounced differences can be found by observing the SEM images of the Li||Cu battery which was deposited at an areal capacity of 1 mA h cm^{-2} (Fig. 3(d5 and d6)). This is due to the induction of uniform spherical Li, which resulted in a lower crossover point and higher CE (98.2% on average). Furthermore, this improvement in battery performance is also evident in assembled Li–S full batteries (Fig. 3(e–g)), where high CE and cycle stability are observed. The discovery also highlights another advantage of spherical Li over other Li deposits, namely, its minimal surface area per unit volume. This characteristic leads to a reduced area of contact between the electrolyte and fresh Li, resulting in a decreased formation of the SEI interface. Consequently, this phenomenon contributes to higher CE and an extended cycle life.

With the advancement and diversification of technology, spherical Li deposition has gradually appeared in the public's vision and shown better development. It is designed to promote the formation of smooth and uniform sediment layers with minimal area to improve circulation performance and ensure safety issues. For instance, in 2020, Zhu *et al.*[98] employed Ag as a modifier on Cu foil to create a spherical island model for enhancing the deposition of Li with smooth surface (Fig. 4a). Initially, the globular Ag nuclei facilitate the reduced nucleation potential of deposited Li atoms. Subsequently, Li uniformly grows around these spherical islands to form a flat surface layer, which is opposite to the irregular growth observed on pure Cu foil. The SEM comparison image after 120 cycles (Fig. 4b) further indicates that the electrode formed using Ag nanoparticles wrapped around 3D copper foam combined with molten Li (Li-ANCF) exhibits smoother surfaces with no dendrite formation. Undoubtedly, the rate performance when using the Li-ANCF electrode surpasses that of the electrode produced by melting Li on bare copper foil (Li-BCF) (Fig. 4c). In the same year, Wang *et al.*[99] successfully achieved uniform dispersion of carbonized metal–organic frameworks (MOFs) of nanosized Co coated by N-doped graphene (Co@N-G). This material effectively enhances graphene's affinity for Li, while the unique cubic hexahedral structure facilitates the formation of spherical Li during Li deposition, thereby promoting a more stable deposition/stripping process. The remarkable advantage of the Co@N-G electrode can be observed in both the CE image (Fig. 4e) and the Li magnification test (Fig. 4f), which is closely associated with its ability to facilitate spherical Li deposition. To summarize, the presence of spherical Li deposition effectively inhibits adverse effects caused by irregular dendrites and enables a stable long-cycle performance with high efficiency.

3.2. Acquisition of spherical Li

The distinct characteristics of spherical Li, such as its non-tip shape and the promotion of SEI formation to minimize the low barrier, have significantly propelled LMBs toward a new direction.[100,101] Currently, despite numerous reports on inducing spherical Li deposition and achieving efficient and stable circulation,[102,103] there is a comprehensive interpretation of obtaining spherical Li deposition. It is well known that a number of variables, including areal capacity, current density, and electrolyte, lead to different Li deposition morphologies.[104,105] Thus, it is possible to effectively regulate spherical Li deposition by taking these important aspects into account. Furthermore, this part provides a systematic overview of the existing literature on the formation of spherical Li deposits and elucidates the

 This journal is © The Royal Society of Chemistry 2025

Published on 30 mis Genver 2025. Downloaded on 19/04/2026 22:10:03.

underlying factors contributing to diverse morphologies of Li deposition, thereby facilitating enhanced control over Li deposition morphology.

3.3. Factors affecting the formation of spherical Li

(1) Electrolyte additives. Li deposition in batteries involves a more intricate situation compared to standard metal deposition. Interfacial energy will change with the additives, paired anions, and molecules of aprotic solvent adsorbed on deposited Li. Moreover, the presence of the SEI layer further complicates this phenomenon. Previously, some reports have proved that the electrolyte and the SEI layer formed could have an obvious influence on the Li deposition morphology, and these studies have also focused on the mechanism of this correlation.[56,106–108] By observing the effect of the type and composition of electrolytes on the Li deposition morphology, it is found that the addition of appropriate organic/inorganic additives is conducive to the formation of circular sediments.

In the research on electrolytes for Li batteries, different types of electrolyte additives have been employed for the purpose of improving different properties of various kinds of LMAs. Among them, film-forming additives are one of the most widely studied and representative strategies for stabilizing SEI films. For example, 1,3-propane sultone (1,3-PS), fluorinated ethylene carbonate (FEC), and vinylene carbonate (VC) have been added to Li batteries, which all contribute to the formation of a robust SEI film on the surface of Li anodes. Undoubtedly, these additives have contributed to the promotion of Li batteries but have played little role in obtaining spherical Li deposits (Fig. 5(a)).[109,110] With the development of this area, $LiNO_3$ is widely recognized as a "prominent" film-forming additive to control the dissolution sheath of electrolytes, forming nitrogen-containing SEIs, which can change the morphology of deposited Li and thereby improve the cycle stability of LMAs.[111] Importantly, the introduction of $LiNO_3$ can cause Li deposition to grow in the form of spherical particles. To be honest, this feature is effective for LMBs; however, for Li–sulfur batteries, the deposition of spherical Li cannot be fully achieved through the sole use of $LiNO_3$, which requires the additional introduction of polysulfides to play a synergistic role. For example, the combined effect of $LiNO_3$ and Li polysulfide in inhibiting dendrite development, explored by Li *et al.* in 2015,[2] demonstrated that only using $LiNO_3$ as the additive to the electrolyte was not sufficient to inhibit dendrite growth effectively. As can be seen in Fig. 5(b), in the case where $LiNO_3$ alone is incorporated, the SEI film formed by the electrolyte without polysulfide is of insufficient mechanical strength, resulting in cracks and pits where Li filaments grow. In contrast, supplementation of electrolytes with polysulfide (Li_2S_8) diminishes Li nucleation sites within the electrolyte through the reaction between metallic Li anode and Li_2S_8, thereby facilitating flattened deposition of Li. Based on the SEM pictures (Fig. 5(c)), the current density is 2 mA cm^{-2}, and the Li deposition capacity is 0.2, 2, and 6 mA h cm^{-2}, respectively. When only $LiNO_3$ is introduced into the electrolyte, Li filaments can be seen to varying degrees (Fig. 5(c1, c3 and c5)). As shown in Fig. 5(a), filaments gradually grow out of the spherical particles. As Li deposition continues, large areas of filamentary Li spread over the surface (Fig. 5(c)). These structures are not only a threat to the safety of the battery but also lead to a higher dead Li stripping rate. In contrast, due to the combined effect of $LiNO_3$ and polysulfides, the substrate surface is gradually covered by flat circular Li deposits with uniform distribution and no obvious Li-shaped stacking (Fig. 5(c2 and c4)). Fig. 5(c6) shows the appearance of long filamentary dendrites that could be connected to the cyclic areal capacity and current density. In addition, the introduced O_2 at the cathode side also favors the formation of spherical Li, according to the literature published by Shi *et al.* in 2017.[112] As illustrated in Fig. 5(d), other conventional Li batteries produce disorganized whisker-like Li at different current densities (0.1 and 1 mA cm^{-2}) with the same areal capacity of 1 mA h cm^{-2} (Fig. 5(d1–d4)). In contrast, SEM images of the LMA with the same electrolyte composition in Li–O_2 batteries depicted in Fig. 5(d5 and d6) reveal a circular morphology and a uniform distribution of Li deposits, which confirm the important role of introduced O_2.

To sum up, the incorporation of strong inhibitors such as $LiNO_3$ and Li polysulfide promotes the formation of dense spherical Li morphology while minimizing the surface area, thereby mitigating electrolyte consumption and dead Li accumulation, ultimately leading to improved cycling efficiency. Furthermore, other components (O_2 and polysulfides) also facilitate the adhesion of these spherical Li deposits.[113]

(2) Electrolyte components. Common electrolytes can mainly be divided into ether-based and carbonate-based electrolytes. In ether-based electrolytes, the SEI membranes consist of flexible oligomers, which confer a natural advantage in the

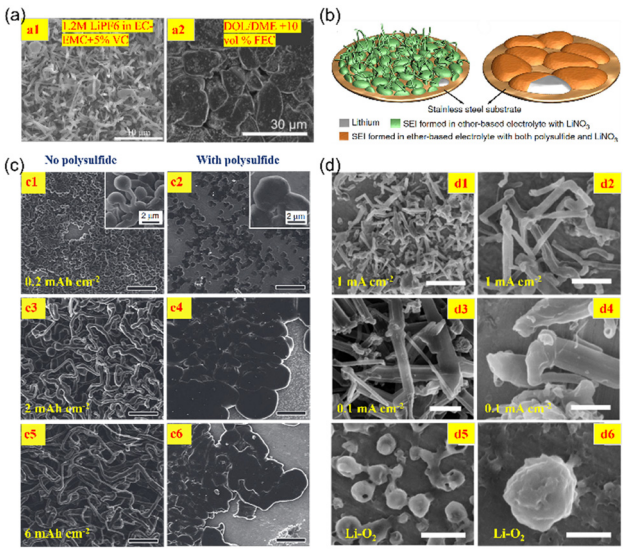

Fig. 5 (a) Li deposition morphology after adding mold-forming additives (a1) VC[109] and (a2) FEC[110] to different types of electrolytes. (b) Illustration of Li deposited morphologies in various electrolytes. (c) SEM images of Li deposition on a stainless-steel substrate.[2] (d) SEM images of deposited Li at different current densities and Li–O_2 battery. (Scale bars: d1, d3 and d5, 5 μm; d2 and d4, 2 μm; d6, 1 μm.)[112]

Published on 30 mis Genver 2025. Downloaded on 19/04/2026 22:10:03.

stability of negative electrodes, making these electrolytes particularly suitable for processing highly active anode materials. However, when ether-based electrolytes are employed alone in full cells, Li whiskers are inevitably formed during the continuous cyclic reactions. As indicated in Fig. 6(a1 and a2), dendritic deposition was found in 1 M LiTFSI containing 1,3-dioxane/1,2-dimethoxyethane (DOL/DME, 1 : 1 v/v), which is a typical ether-based electrolyte, and the stacking of clumped Li deposits was found ((as shown in the zoomed-in view) which might be due to the outstanding anode stability of the ether-based electrolyte itself.[114] Fortunately, spherical Li deposits can generally be achieved through the addition of specific additives, such as $LiNO_3$, to ether-based electrolytes, as described in the study of Li deposition morphology in different electrolytes by Shi *et al.* in 2017.[112] Specifically, they demonstrated that incorporating 1% $LiNO_3$ into an electrolyte comprising DOL/DME (in the ratio of 1 : 1 v/v) within a 1 M LiTFSI solution successfully transformed Li deposition morphology into a spherical shape (Fig. 6(a3 and a4)). In addition, uniform round Li deposits were also obtained at higher current densities when additional polysulfides at a concentration of 5 M were added to the Li–S full cell to form the cathode solution for electroplating, as shown in Fig. 6(a5 and a6). This finding is in agreement with the previous report by Li *et al.*[2] Unfortunately, despite their advantages, the poor oxidative stability of ether-based electrolytes significantly restricts their applicability in batteries with high-voltage cathodes ($\geq$4.3 V).[115–117] In contrast, carbonate-based electrolytes possess higher anodic potentials and lower flammability profiles, which make them much more compatible than ether-based electrolytes for high-voltage cathodes. Similarly, as shown in Fig. 6(a7 and a8), significant dendrites appeared when the electrolyte was 1 M $LiPF_6$ containing 1 : 1 v/v EC/DEC, without additional additives. According to Liu *et al.*'s research,[60] introducing certain amounts of $LiNO_3$ into this carbonate matrix resulted in well-defined spherical Li deposits (Fig. 6(b)). However, the solubility of $LiNO_3$ is limited ($<10^{-5}$ g mL^{-1}) in carbonate-based electrolytes, which has greatly hindered its application in traditional carbonate electrolytes.[118–120] In order to solve this problem, Liu *et al.*[60] designed a solubility-mediated slow-release mechanism wherein nanoparticles of $LiNO_3$ are embedded within a porous polymer framework on the anode surface and gradually dissolve when running the battery as soluble forms are consumed as shown in Fig. 6(c). Fig. 6(d) illustrates unique morphological evolution characterized by spherical growth patterns distinct from those associated with dendritic formation typically seen under nitrogen oxide-saturated conditions in carbonate environments. In addition, the performance of the electrolyte employing dissolved $LiNO_3$ was significantly improved compared to the other two electrolytes (Fig. 6(e)). Other methodologies aimed at enhancing solubility levels concerning $LiNO_3$ have been documented elsewhere but will not be reiterated here.[121–124]

It is noteworthy that Luo *et al.*[125] have developed a composite electrolyte (nitrocellulose (NC) combined with Li bis(fluorosulfonyl)imide (LiFSI)) which showed excellent reversible properties in lean electrolyte cells under the conditions of high current density. Fig. 7(a) demonstrates that an inorganic LiF-rich layer was formed promoted by LiFSI, and NC played the role of a passivated organic layer which encapsulated the above inorganic layer. This joint effect of the nitro group in NC and the LiF-rich interface facilitates even plating/stripping of Li,

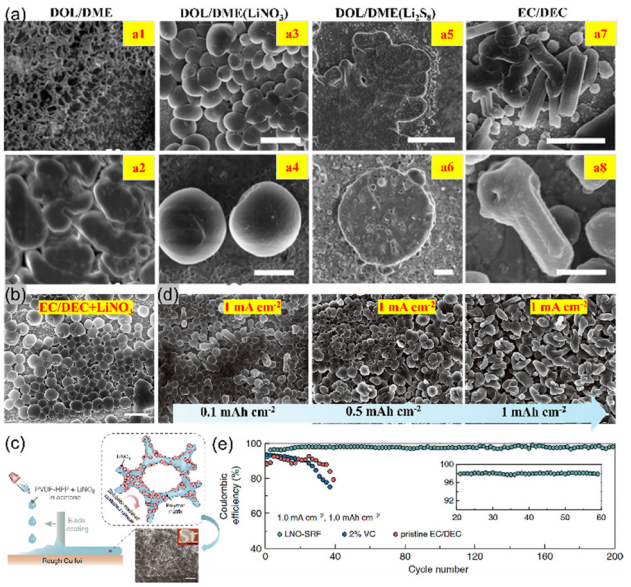

Fig. 6 (a) The morphologies of deposited Li in different electrolytes at 0.1 mA cm^{-2} and 1 mA h cm^{-2}.[112,114] (b) The morphologies of deposited Li in a 1.0 M $LiPF_6$ EC/DEC electrolyte with saturated $LiNO_3$. (c) Illustration of the fabrication and working process of a freestanding membrane consisting of $LiNO_3$ dissolved in a polymeric matrix (termed $LiNO_3$ sustained-release film, LNO-SRF). (d) The morphologies of deposited Li on a Cu substrate covered by LNO-SRF. (e) CE at 1 mA cm^{-2} and 1 mA h cm^{-2} in different electrolytes.[60]

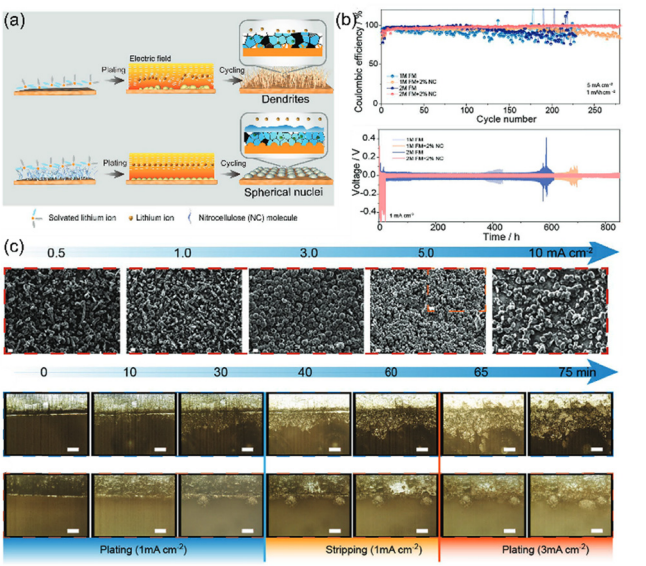

Fig. 7 (a) Schematic diagram of dendritic/spherical Li deposition. (b) The CE of Li||Cu and Li||Li cells and the cyclic performance of Li||Li cells at 1 mA cm^{-2} and 1 mA h cm^{-2}. (c) Deposited Li in different electrolytes.[125]

This journal is © The Royal Society of Chemistry 2025

Published on 30 mis Genver 2025. Downloaded on 19/04/2026 22:10:03.

leading to the formation of spherical nuclei of Li even at elevated current densities. With this advantage, LMBs showed excellent electrochemical performance (Fig. 7(b)). Furthermore, Fig. 7(c) illustrates the SEM images of the Li crystal nucleus under different current densities between 0.5 and 10 mA cm^{-2} at a fixed areal capacity of 0.1 mA h cm^{-2}. Interestingly, when 2% NC is added, the Li nucleus changes from rod to ball with the increase of current density. In the morphological evolution diagram of the electroplated/stripped Li electrodeposited layer observed through *in situ*/*ex situ* techniques at various current densities, it is observed that Li metal assumes a spherical morphology when applied at a high current density (>1 mA cm^{-2}) in a 2 M LiFSI/DME(FM) + 2% NC electrolyte.

(3) Current density and areal capacity. It is widely acknowledged that current density and areal capacity affect the behavior of deposited Li significantly. To regulate the ordered deposition of Li spheres, exploring the deposition behavior of Li under different current densities and areal capacities and finding the most favorable operating conditions for the formation of Li spheres are indispensable. According to the investigation, a considerable number of spherical Li that emerged in some studies might be associated with the utilization of ether electrolytes or with the additives, but the morphological disparity of the Li deposits resulting from different current densities cannot be disregarded. In 2017, Pei *et al.*[93] analyzed the deposition behavior of Li metal on a planar copper electrode by using different current densities or areal capacities in an ether electrolyte containing the $LiNO_3$ additive. The conclusions drawn are presented in Fig. 8(a), according to which the diameters of the Li nucleus are proportional to the reciprocal of electrochemical overpotential, and the number density of the Li nucleus is proportional to the cubic power of the electrochemical overpotential. Specifically, Fig. 8(b) reveals the morphology of deposited Li at different current densities (0.025–10 mA cm^{-2}) under an areal capacity of 0.1 mA h cm^{-2}. At lower current densities (Fig. 8(b1and b2)), Li grows larger on the copper electrode surface and diffuses thinly because Li atoms are prone to deposit on the existing nucleus instead of re-forming a new nucleus at low current. Consequently, the Li nuclei come into contact and fuse with each other and pack tightly together as the current density exceeds 1 mA cm^{-2}, which validates the conclusion of Fig. 8(a). Additionally, Fig. 8(c) indicates more comprehensive SEM images under different current densities or areal capacities, which further substantiate the obtained theory and offer an effective reference for the subsequent design and formation of uniform Li ball deposits.

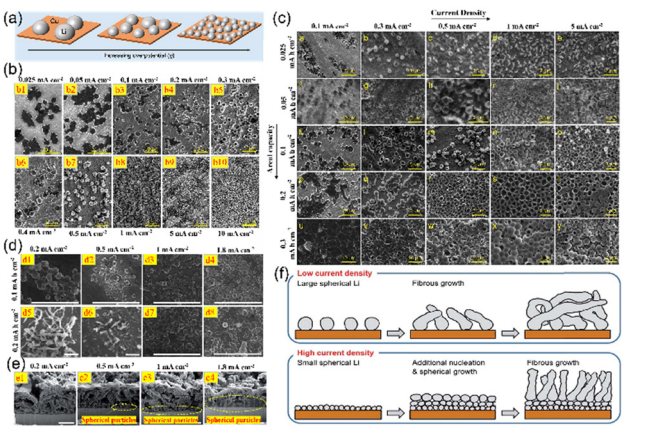

Fig. 8 (a) Illustration of the density and size of Li nuclei at different overpotentials. (b) Morphologies of deposited Li at various current densities between 0.025 and 10 mA cm^{-2} at an areal capacity of 0.1 mA h cm^{-2}. (c) Morphologies of deposited Li at different current densities and areal capacities.[93] (d) Morphologies of deposited Li at the areal capacity of 0.1 and 0.2 mA h cm^{-2} at various current densities. (e) Cross-sectional images of deposited Li at an areal capacity of 1 mA h cm^{-2} with different current densities. (f) Illustration of the evolution of morphology.[126]

Additionally, in 2021, under identical experimental conditions (DOL/DME with 1 wt% $LiNO_3$, deposited on copper foil), Lee *et al.*[126] not only investigated the disparity of Li deposition behavior with the alteration of current density and areal capacity but also indicated that the dendrite Li phenomenon would arise with the increment of deposition amount. As depicted in Fig. 8(d), at the beginning with a current of 0.1 mA h cm^{-2}, the size of Li nuclei reduces, and the size increases with increasing current density, which is in agreement with the conclusion of Pei's results. Nevertheless, with the augmentation of the amount of electrodeposition, dendrite Li emerges at lower current densities (Fig. 8(d5 and d6)), while at 1.0 and 1.8 mA cm^{-2}, multiple layers of spherical Li are covered on the Cu substrate compactly, as well as the particle size of Li increases vertically from bottom to top. When the areal capacity increased to 1 mA h cm^{-2} (Fig. 8(e)), only filamentous deposition of Li existed at 0.2 mA cm^{-2}, and when the current density gradually increased from 0.5 mA cm^{-2} to 1.8 mA cm^{-2}, there were spherical Li particles grown on the copper surface, combined with sparse Li spheres and multi-layer Li spheres. However, when the spherical Li particles grew to a certain extent, that is, when they reached a certain size, the Li particles transformed into fibrous growth, which is decided by the electrochemical environment of the cell. As illustrated in Fig. 8(f), since the stress was released when spherical Li was converted into columnar deposition, Li would be preferentially deposited onto the formed fibrous Li, while for the smaller Li balls, they remain unchanged. Consequently, only filamentous Li deposits exist at a low current density, and their diameters and lengths are large. When operated using a preset high current density, the Li particles grow spherically during the initial nucleation on the surface of the substrate. And the Li nuclei can grow without becoming coarse under the dynamic boundary conditions. However, with the growing of the particle, the base-controlled growth mechanism can be used to explain the electrodeposition conditions, which causes the Li deposits to deform and cause columnar growth plastically. In view of this phenomenon, Lee's research group made improvements on this basis to induce uniform and compact columnar Li deposition, which will be elaborated in the next section.

Nevertheless, in traditional carbonate electrolytes, the deposition of Li might differ from the aforementioned research findings. For instance, in 2021, Dong *et al.*[127] disclosed that the low local current distribution during the deposition of Li is

Published on 30 mis Genver 2025. Downloaded on 19/04/2026 22:10:03.

more beneficial for the formation of compact spherical Li. Specifically, by observing the SEM image depicted in Fig. 9(a), the spherical Li (approximately 500 nm) is identified when the deposition amount is 1 mA h cm^{-2} at 0.2 mA cm^{-2} (Fig. 9(a1 and a2)). Some of the smaller spheres found in the enlarged image might be newly formed Li electrodeposits, which would continue to expand if the electrodeposition proceeds. Subsequently, with the increase of current density, the Li deposition becomes increasingly uneven, and spherical Li and columnar Li coexist.

Spherical and dendritic structures are more pronounced at higher current densities (5 and 10 mA cm^{-2}). This phenomenon can be accounted for by the space charge theory, namely, current densities below J_{lim} (2.1 mA cm^{-2}) can give rise to relatively flat deposits, while those above J_{lim} lead to dendritic deposits. By inspecting their internal structure, it can also be discovered (Fig. 9(b)) that spherically stacked uniform and compact structures emerge at 0.2 mA cm^{-2} (Fig. 9(b1 and b3)), in contrast with the shrubby electrosedimentary layer at 5 mA cm^{-2} (Fig. 9(b2 and b4)). Based on these outcomes, the Li electrodeposition and growth processes in the carbonate-based electrolyte should comply with the mechanism diagram in Fig. 9(c). That is, at a low deposition rate, Li^+ is distributed relatively evenly, and Li spheres can arise adjacent to the electrode surface and accumulate with the deposition. Conversely, once the critical rate is surpassed, the Li deposition occurs in a disordered manner, and the coexistence of spherical Li and shrub-like Li is found.

In conclusion, the role of electrolyte additives, electrolyte components, and current density/areal capacity in Li deposition morphology was analyzed, and the operating conditions conducive to the formation of spherical Li morphology were summarized. This will also effectively facilitate the subsequent obtaining of Li spheres.

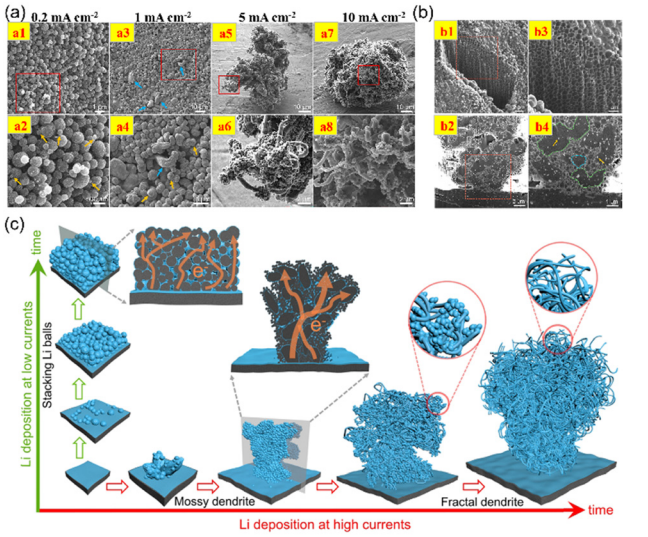

Fig. 9 (a) Morphologies of deposited Li at various current densities ranging from 0.2 to 10.0 mA cm^{-2} at an areal capacity of 1.0 mA h cm^{-2}. (b) Internal view of the granular and bush-shaped Li obtained by FIB/SEM. (c) Illustration of the deposited Li at different currents.[127]

3.4. Nucleation and growth mechanisms of spherical Li

Spherical Li deposition can effectively prevent the severe safety risks caused by dendritic Li formation. The previous section elaborates on the strategies for regulating the formation of spherical Li deposits; however, the formation mechanisms of spherical Li are still not well comprehended. The elucidation of the formation mechanism of Li balls can further guarantee the realization of safe and stable LMBs. In this respect, Zhang *et al.* developed a mechanism of diffusion–reaction competition for Li^+, which achieves the deposition of Li in different scenarios by dividing the controlling step of Li deposition into two categories, namely diffusion and reaction.[128] Typically, the deposition of Li occurs below the SEI coating. This involves Li^+ passing through the SEI film and gaining electrons to convert into Li atoms. However, as shown in Fig. 10(a), when the diffusion rate decreases throughout the Li deposition process with the same electrode reaction rate, it becomes difficult for Li^+ to pass through the SEI film, which is referred to as a sluggish SEI. Concurrently, the reduction of ions will lead to a shortage of Li^+ below the SEI, which is referred to as the diffusion-controlled mechanism.

As a result, there is a lack of Li^+, and they tend to gather at the tips, leading to the formation of dendritic Li deposits. In the opposite, in the case of fast SEI, the nucleation of Li will occur under the SEI and spherical Li will be achieved. In order to validate this diffusion–reaction mechanism, Chen *et al.*[128]

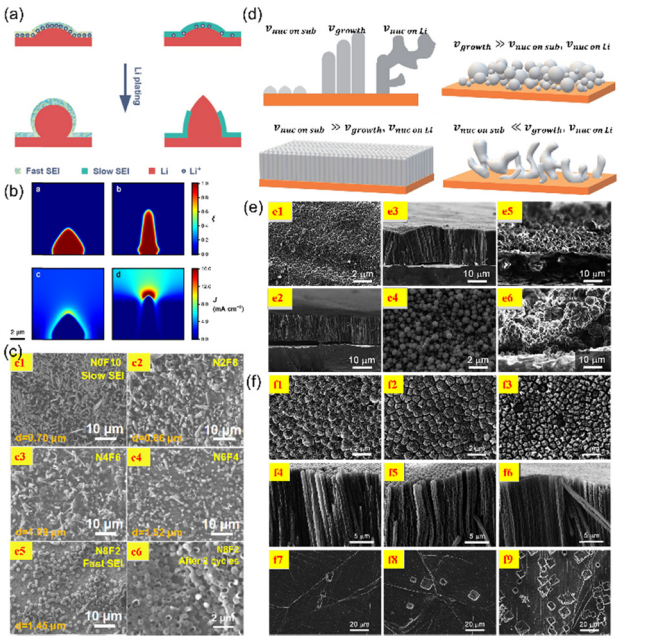

Fig. 10 (a) Illustration of dendritic/spherical deposition of Li under slow and fast SEI. (b) Li deposition morphology and local current density distribution from phase field modeling. (c) SEM images of dendritic/spherical Li deposition at a current density of 0.50 mA cm^{-2} and an areal capacity of 0.125 mA h cm^{-2} in different electrolytes.[128] (d) Illustration of the reaction rates at different electroplating steps. (e) Morphologies of deposited Li in the electrolyte of $LiPF_6$ dissolved in EC/DEC at a current density of 0.1 mA cm^{-2} under different capacities. (f) Top-view of columnar metallic Li after stripping under different areal capacities.[129]

 This journal is © The Royal Society of Chemistry 2025

Published on 30 mis Genver 2025. Downloaded on 19/04/2026 22:10:03.

employed a phase field model to replicate the spherical/dendritic formation of Li during rapid/slow SEI deposition.

As shown in Fig. 10(b), it is evident that in situations where diffusion is the controlling factor, Li^+ faces obstacles in diffusing through the SEI layer. This leads to the accumulation of local current density at the tip, indicating the formation of dendritic structures. In contrast, when the reaction control dominates, spherical Li deposits are created successfully accompanied by even local current densities around the spherical Li. This characterization technique can be widely employed in the subsequent investigation of spherical Li and can clearly emphasize the production of spherical Li. In addition to the physical field model, Zhang *et al.* also employed a series of electrolytes in DOL/DME containing 1.0 M $LiNO_3$ and LiTFSI as a model system for constructing SEI with a diffusion kinetic gradient. Conventional $TFSI^-$ partially substitutes NO^{3-} to generate Li_3N and LiN_xO_y in the SEI film, and thereby increases the Li^+ conductivity of the SEI film. Specifically, the electrolytes with different molar ratios of $LiNO_3$: LiTFSI at 0 : 10, 2 : 8, 4 : 6, 6 : 4, and 8 : 2 were utilized to form SEI with enhanced ionic diffusion coefficients. Fig. 10(c1–c5) presents the SEM images of deposited Li on Cu foil at 0.5 mA cm^{-2} and 0.125 mA h cm^{-2}. With the escalation of the molar ratio of $LiNO_3$ and LiTFSI, spherical Li deposits gradually emerge. When the N8F2 ($LiNO_3$: LiTFSI = 8 : 2) electrolyte is utilized, all Li atoms have the tendency of depositing in the form of spheres. The gradual spherical Li deposition here is for the reason that with the increase of the diffusion rate of Li^+, the ion concentration under the SEI film with the same electrode reaction rate increases. Additionally, the morphology of Li deposition in the N8F2 electrolyte after two plating/stripping processes (Fig. 10(c6)) is also observed to maintain a spherical structure, indicating that the deposited Li morphology is constantly controlled by adjusting the competition between diffusion and reaction processes.

In addition to the aforementioned diffusion–reaction mechanism, there is another fascinating query. Lee[129] also elucidated the formation mechanisms of columnar Li metal, multilayered spherical Li accumulation, and dendrite Li based on the rates of Li nucleation on the substrate, Li growth and Li nucleation on Li (Fig. 10(d)). Among them, ordered columnar Li deposition represents the optimal state for forming a dendrite-free anode, which can effectively avert the safety hazards caused by dendrite Li. Specifically, when the rate of Li nucleation on the substrate ($V_{\text{nuc on sub}}$) exceeds the rate of Li growth (V_{growth}) and Li nucleation on Li deposits ($V_{\text{nuc on Li}}$), the Li nuclei will first grow on the substrate rather than form metallic Li. Thus, with the increase of areal capacity, one-dimensional growth of Li occurs, leading to the formation of columnar Li metal. However, if V_{growth} surpasses $V_{\text{nuc on sub}}$ and $V_{\text{nuc on Li}}$, the deposition of Li nuclei will be hard to see, and the metallic Li grows in every direction as the continuous plating of Li, resulting in the formation of multiple layers of spherical Li. Eventually, when $V_{\text{nuc on Li}}$ is greater than $V_{\text{nuc on sub}}$ and V_{growth}, the Li metal is more prone to deposit at the surface of formed Li instead of depositing at the surface of the substrate. Therefore, during operating, the Li metal grows randomly in the form of dendrites. Simultaneously, the SEM images of the surface/cross-section of various substrates, namely the Cu foil (Fig. 10(e1–e3)) and the Ti foil (Fig. 10(e4–e6)), at 0.2, 4, and 6 mA h cm^{-2} were characterized. At 0.2 mA h cm^{-2}, the Li nucleus on Cu foil is denser and smaller than that on the Ti foil, and the disparity becomes more pronounced with the augmented deposition amount. This reveals that a hetero-nucleation rate is associated with the different substrates, namely, a faster hetero-nucleation rate is associated with the deposition of regular columnar Li metal. Finally, the role of columnar Li metal in enhancing electrochemical performance compared with traditional Li metal was elucidated by comparing the morphological alterations of the Li metal cylinder with traditional metallic Li electrodes in terms of the exfoliation process of Li. Fig. 10(f1–f3) and (f4–f6) present the different views (top and cross-section) of the Li cylinder electrode when stripping under 0.1 mA cm^{-2}. With the increase in the stripping amount, each Li metal cylinder shrinks uniformly, indicating that the exfoliation process of Li metal across the whole electrode surface occurs uniformly. On the other hand, non-uniform stripping phenomena were witnessed when using the traditional Li metal electrode, and the area of the pores enlarged gradually following the increase in the stripping amount, as depicted in Fig. 10(f7–f9).

4. Combining spherical Li with conductive 3D frameworks

As discussed above, the main challenges of LMAs are Li dendrite growth and infinite volume expansion. Although spherical Li can effectively address the dendritic Li formation, the volume expansion problem still needs to be solved.[130–134] Fortunately, the 3D conductive frameworks have high mechanical robustness and flexibility to withstand the volume changes that occur during charging/discharging.[135–140] The combination of the 3D conductive frameworks and spherical Li may have a profound influence on improving the inhibition of the volume change and Li dendrite growth of the LMA.

However, frequently employed 3D skeletons (Cu foam, Ni foam (NF), carbon cloth (CC), *etc.*) exhibit lithiophobic characteristics.[141–143] Therefore, there is a necessity of depositing lithiophilic materials on the surface of these 3D skeletons. Various methods have been developed to uniformly coat these materials on the skeleton, such as magnetron sputtering,[144] vapor phase deposition,[145] aqueous metal salt treatment,[146] atomic layer deposition,[147] and the use of metal–organic framework (MOF) derivatives.[148] Among them, using MOF derivatives to fabricate the lithiophilic 3D frameworks shows significant advantages in the above-mentioned techniques, which can be referred to in our previous review.[149]

Unfortunately, it seems still difficult to acquire spherical Li in these monometallic MOF derivative modified 3D frameworks. For example, in the previous study of our group, a MOF-derived (ZIF-67) Co_3O_4 layer was uniformly coated on the NF framework and injected with molten Li to obtain a Li–Co_3O_4-NF composite anode (Fig. 11(a)).[150] In ether electrolytes, the anode demonstrated

Published on 30 mis Genver 2025. Downloaded on 19/04/2026 22:10:03.

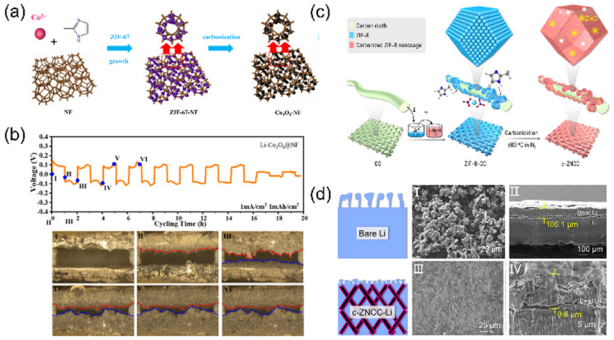

Fig. 11 (a) Synthesis procedure of the Co_3O_4-NF electrode.[150] (b) *In situ* OM tests of the Li–Co_3O_4-NF symmetric cells. (c) Illustration of the preparation of c-ZNCC.[151] (d) SEM images of c-ZNCC-Li and bare Li anodes after cycling for 500 cycles.

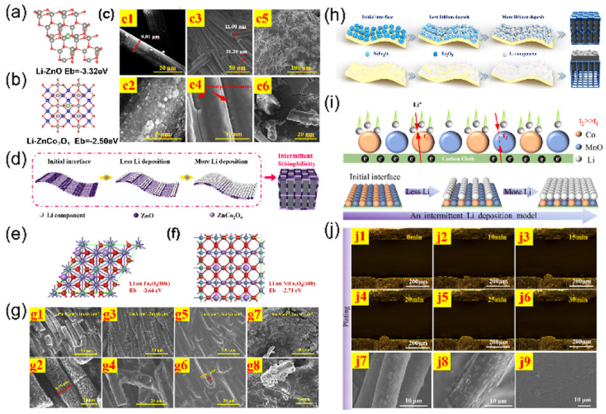

Fig. 12 (a) and (b) DFT calculation of binding energies of Li atoms with ZnO and $ZnCo_2O_4$. (c) SEM images of plated Li on CC@ZZCO under different capacities. (d) Schematic of Li interstitial deposition consisting of ZnO and $ZnCo_2O_4$.[152] (e) and (f) DFT calculation of binding energies of Li atoms with Fe_2O_3 and $NiFe_2O_4$. (g) Li encapsulation process of the CC@NFFO skeleton under different capacities. (h) Illustration of Li interstitial deposition consisting of Fe_2O_3 and $NiFe_2O_4$.[153] (i) Illustration of Li interstitial deposition consisting of MnO and Co. (j1)–(j6) *In situ* OM of Li deposition on CC@MnO/Co/C. (j7)–(j9) SEM images of plated Li on CC@MnO/Co/C under different capacities.[154]

relatively uniform Li deposition behavior. Nevertheless, the growth of Li dendrites was still found by using *in situ* optical microscopy (OM) (Fig. 11(b)). Zhuang *et al.* synthesized c-ZNCC (ZnO, N binary doped nanocages) as the main body of the LMA using ZIF-8 (zeolite imidazolate framework-8) (Fig. 11(c)).[151] The anode has excellent cycling stability and efficient charge/discharge capability. However, regarding the morphology of the surface of this anode after cycling, the formation of dendritic Li cannot be avoided, although the thickness of c-ZNCC-Li had been significantly reduced (Fig. 11(d)).

Interestingly, while utilizing bimetallic MOF derivatives to fabricate lithiophilic 3D frameworks, spherical Li deposition behavior can be clearly seen without changes of the electrolyte components or any electrolyte additives. For instance, based on our previous study, the formation of spherical Li was clearly found on the surface of a lithiophilic framework constructed based on ZnCo-MOF derivatives ($ZnCo_2O_4$ and ZnO) (CC@ZZCO).[152] This phenomenon was first theoretically supported by DFT calculations, which showed that ZnO has a stronger affinity for Li adsorption and nucleation (Fig. 12(a and b)). It is demonstrated that Li prefers preferential nucleation and growth on ZnO. To investigate the Li deposition behavior further, we conducted Li deposition experiments at 1 mA cm^{-2} under various areal capacities (Fig. 12(c1–c4)). When operating under 5 mA h cm^{-2}, Li deposited on the CC formed small protrusions aligned along the fiber direction and presented a spherical Li morphology (Fig. 12(c1 and c2)). The spherical Li was densely arranged on the CC surface, which inhibited the growth of Li dendrites effectively. As the deposition time increases (under 10 mA h cm^{-2}), Li deposition begins to abandon the protruding regions and instead fills the surface (Li deposition on $ZnCo_2O_4$), eventually forming a smooth surface (Fig. 12(c3 and c4)). Furthermore, the diameter was 8.69 μm for the original CC, which increased to 9.81 μm after deposition at 1 mA cm^{-2} with the capacity of 5 mA h cm^{-2} for CC@ZZCO; with more Li deposition, the diameter increased to about 11.00 μm. This indicates that most of the deposited Li are formed on the CC instead of forming large clumps or dendrites at the top of the framework. Nevertheless, when deposited on pure CC under the same current deposition conditions, Li exhibited a disordered stacking morphology (Fig. 12(c5 and c6)). This phenomenon further proves that CC@ZZCO can induce the uniform nucleation of Li effectively. The specific mechanism is shown in Fig. 12(d), where $ZnCo_2O_4$ and ZnO are intermittently aligned on the CC, which contributes to guiding the uniform deposition of Li.

Similarly, in another study also conducted by our group, a lithiophilic framework (CC@NFFO) was constructed based on bimetallic NiFe-MOF derivatives (Fe_2O_3 and $NiFe_2O_4$).[153] The binding energies of both Fe_2O_3 and $NiFe_2O_4$ were demonstrated to be lower than that of graphitic carbon (−1.63 eV) using DFT calculations (Fig. 12(e and f)), which illustrated the strong lithiophilicity of both of them. Furthermore, since the binding energy of $NiFe_2O_4$ (−2.71 eV) is higher than that of Fe_2O_3 (−3.64 eV), the Li atoms are adsorbed on Fe_2O_3 prior to the adsorption onto $NiFe_2O_4$. Equally, we electrodeposited different amounts of Li at 1 mA cm^{-2} (Fig. 12(g)) and at an areal capacity of 1 mA h cm^{-2}; as shown in Fig. 12(g1 and g2), there is a dense granular arrangement, demonstrating that Li atoms are preferentially deposited in the Fe_2O_3 region. Subsequently, Li atoms were deposited in the $NiFe_2O_4$ residual zone (Fig. 12(g3 and g4)). It culminated in the uniform Li deposition on the smooth skeleton surface at 8 mA h cm^{-2} (Fig. 12(g5 and g6)). However, the bare Li electrode morphology (Fig. 12(g7 and g8)) revealed that the disordered nature of Li led to its random deposition on the CC and aggregation. The Ni and Fe metal atoms from NiFe-MOFs are separated by organic ligands, while their derivatives could maintain the structure of the MOFs, and the intermittent distribution of Fe_2O_3 and $NiFe_2O_4$ on the CC facilitates homogeneous deposition (Fig. 12(h)). In contrast, the deposition of Li on the bare CC surface resulted in the growth of Li dendrites. Therefore, the model not only avoids the Li ion accumulation issue, but also maximizes the role of the 3D skeleton and achieves high-capacity maintenance.

 This journal is © The Royal Society of Chemistry 2025

Published on 30 mis Genver 2025. Downloaded on 19/04/2026 22:10:03.

What's more, our recent work also found the presence of spherical Li deposition, where the 3D framework consisted of intermittent arrangements of Co and MnO derived from Mn-Co bimetallic MOFs.[154] Since the conductivity of Co is higher than that of MnO, it can be hypothesized that electrons conduct faster in Co, and therefore Li atoms preferentially nucleate on the surface of Co, followed by nucleation on MnO. Based on this theory, we mapped the Li deposition mechanism (Fig. 12(i)). In the present study, the nucleation process of Li was observed by *in situ* OM (Fig. 12(j1–j6)). It was observed that the electrode surface was initially flat; when little metallic Li was deposited, Li ions readily nucleated on the surface of Co due to its good electronic conductivity (10 min, tiny lumps). Subsequently, Li intermittently deposited on adjacent small protruding sites (such as MnO), and then the surface of the electrode became flatter (30 min). Consequently, observation of the Li nucleation process by *in situ* OM revealed that Li still tends to form smooth spherical circular shapes on the surface. After the final nucleation, a dense and flat Li film was formed on the surface of the electrode, which promoted the Li deposition stably and effectively avoided the growth of dendritic Li. To analyze this behavior further, we performed Li deposition on an electrode at 1 mA cm^{-2} under various areal capacities and observed the changes in the deposition behavior by SEM. Li was preferentially deposited in a number of rounded blocky areas (Fig. 12(j7)). As the areal capacity increased (Fig. 12(j8)), multiple banded protrusions appeared. Under the situation of 20 mA h cm^{-2}, the electrode surface became smoother without dendrites or interfacial collapse, and the above characterization was in good agreement with the results observed by *in situ* OM (Fig. 12(j9)).

Hence, these three examples of bimetallic MOF derivatives combined with the 3D conductive frameworks (CC@ZZCO, CC@NFFO and CC@MnO/Co/C) confirmed that obtaining spherical Li on these kinds of substrates is not occasional. And the construction of a lithiophilic 3D framework by introducing bimetallic MOF derivatives not only significantly improves the morphology of deposited Li, but also promotes the homogeneous nucleation of Li, which optimizes the long-term stability and cycling performance of the cell and further improves the overall electrochemical performance.

As known to all, in the history of the development of conductive 3D frameworks for LMAs, primarily two models have been proposed, namely the top growth model with homogeneous lithiophilicity (Fig. 13(a))[143,155–157] and the bottom-up growth model with gradient lithiophilicity (Fig. 13(b)).[158–162] However, for the top-growth model, Li prefers to deposit on the surface of the frameworks due to the homogeneous lithophilicity, thus predisposing to the growth of dendritic Li (Fig. 11(a)). To overcome this issue, the bottom-up growth model was developed. For this model, the majority of Li nucleation sites were missed from the top of these frameworks, thus possibly preventing the maintenance of high areal capacity (Fig. 13(b)). Based on the above discussions, we proposed a new model to explain the Li deposition behavior, namely the intermittent lithiophilic model (Fig. 13(c)).[163] This model is consisting of

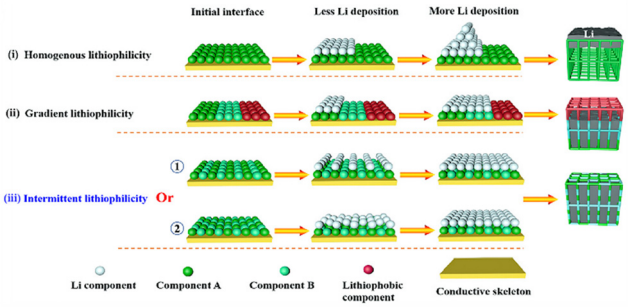

Fig. 13 Schematic diagram of Li deposition behavior on three different conductive 3D frameworks: (a) homogeneous lithiophilic model; (b) gradient lithiophilic model; and (c) intermittent lithiophilic model.[163]

lithiophilic material A and lithiophilic material B which intermittently located on the surface of skeletons in the nano or micro scale where the lithiophilicity of A is stronger than that of B.[152,154,163,164] Since the lithiophilicity of A is superior to B, Li^+ preferentially nucleates and grows on A. Meanwhile, the Li^+ concentration in the electrolyte near A is reduced, combined with the lithiophilicity of B, which will lead to the following nucleation and growth of Li on B. This approach effectively avoids Li accumulation in localized regions while fully utilizing the 3D conducting framework as a nucleation site for Li.

5. Conclusions and outlook

In general, a systematic exploration of the Li deposition process has significantly advanced the development of LMBs. However, to achieve the actual commercialization of LMBs, it is essential to consider the dendrite problem. Spherical Li holds immense potential for advancing highly energy-efficient LMAs. Since neither electrolyte modification nor hosting strategies can completely eliminate dendrites during large-scale practical applications, it is essential to investigate the mechanism for spherical Li deposition so as to seek a new development path to promote LMBs into a higher stage of development. Here, we summarise the key factors affecting spherical Li deposition and the formation mechanism of spherical Li deposition, and conclude by combining the advantages of 3D skeletons to provide inspiration for the future research and development of Li metal batteries.

(1) Influencing factors of spherical Li deposition

Electrolyte additives. Electrolyte additives exert distinct influences on the morphology of Li deposition. Specifically, $LiNO_3$ functions as an effective film-forming additive that modifies the structure of deposited Li, promoting its growth into spherical particles. This modification significantly enhances the cycling stability of LMAs. However, in Li-sulfur batteries, $LiNO_3$ alone is insufficient to achieve fully spherical Li deposition; the presence of additional polysulfides, such as Li_2S_3, is necessary to synergistically facilitate this process. Moreover, introducing oxygen (O_2) on the cathode side further promotes the formation of spherical Li.

Electrolyte composition. Common electrolytes can be classified into ether-based and carbonate-based electrolytes. Spherical

Published on 30 mis Genver 2025. Downloaded on 19/04/2026 22:10:03.

Li deposition is typically achieved by incorporating specific additives, such as $LiNO_3$, into ether-based electrolytes or by adding high concentrations (5 M) of polysulfides to the electroplating cathode solution in Li-sulfur full batteries. However, while spherical Li deposition can be successfully induced by introducing an appropriate amount of $LiNO_3$ into carbonate-based electrolytes, the limited solubility of $LiNO_3$ in these electrolytes ($<10^{-5}$ g mL^{-1}) has hindered its practical application. Consequently, numerous studies have focused on enhancing the solubility of $LiNO_3$ in carbonate-based electrolytes.

Current density and areal capacity. In ether-based electrolytes containing $LiNO_3$ additives, it has been observed that the diameter of Li nuclei is inversely proportional to the electrochemical overpotential, while the number density of Li nuclei is proportional to the cube of the electrochemical overpotential. At lower current densities, Li atoms tend to deposit on existing nuclei, leading to larger and more diffused Li growth on the surface of the copper electrode. However, in conventional carbonate-based electrolytes, a low local current distribution is more conducive to the formation of compact spherical Li.

(2) Mechanism of spherical Li formation

Diffusion–reaction competition. This mechanism categorizes the processes governing Li deposition into diffusion and reaction components. Li deposition typically occurs beneath the SEI layer, involving Li^+ traversing the SEI membrane and acquiring electrons to form Li atoms. When the diffusion rate decreases while the electrode reaction rate remains constant during Li deposition, Li^+ ions face difficulty in crossing the SEI membrane, leading to a deficiency of Li^+ beneath the SEI. At this point, the reduction of ions triggers the aggregation of Li^+ towards the tips of existing deposits, resulting in dendritic Li formation, a phenomenon known as the diffusion-limited mechanism. Conversely, under conditions where the SEI is highly conductive, Li nucleation occurs beneath the SEI, enabling spherical Li deposition.

Mechanism based on nucleation and growth rates. This mechanism explains the formation of columnar Li metal, multilayered spherical Li accumulation, and dendritic Li based on the relationship between the rate of Li nucleation on the substrate ($V_{\text{nuc on sub}}$), the rate of growth (V_{growth}), and the rate of Li nucleation on the Li deposit ($V_{\text{nuc on Li}}$). In this case, if V_{growth} exceeds $V_{\text{nuc on sub}}$ and $V_{\text{nuc on Li}}$, the deposition of Li nuclei is difficult to observe, and as Li continues to be plated, Li metal grows in all directions, leading to the acquisition of multilayered spherical Li.

(3) Combining the 3D conductive frameworks and spherical Li

As discussed above, although spherical Li can address the problems of Li dendrites effectively, the volume expansion still needs to be taken into account for host-less Li. Fortunately, the 3D conductive frameworks are used as supplementary materials to prevent the volume expansion. Thus, the combination of the spherical Li and 3D conductive frameworks may be an effective strategy for obtaining LMAs with excellent electrochemical performances.

In addition, this work summarises several methods to obtain spherical Li, including the addition of electrolyte additives, adjusting the electrolyte composition, varying the current density or surface capacity (Section 3.2.1) and using bimetallic MOF derivatives (Section 4). However, the formation mechanism of spherical Li is far from being well investigated. Therefore, apart from the diffusion–reaction competition mechanism and the rate of Li nucleation, growth and nucleation on Li deposits (Section 3.2.2), other mechanisms which can be used under multi-factors concomitant conditions should also be studied. On the other hand, understanding of the mechanisms of spherical Li deposition can be supported by more advanced *in situ* characterisation. Most of the characterisation techniques carried out to explore the LMA fall into two main categories, *in situ* and *ex situ* techniques. To date, most characterisation studies of the LMA have been performed by non-*in situ* techniques or under static conditions. The development of *in situ* characterisation techniques in real cells under different modes of operation is of great interest and urgency. We fully believe that the combination of these two types of characterisation techniques can facilitate the understanding of the behaviour of spherical Li. On the whole, more efforts should be made to pave the way to the commercialization of LMBs with longer lifespan, higher energy density and safety.

Author contributions

M. T. Wang, X. T. Guo, R. Luo, and X. N. Jiang collected the data, M. T. Wang and X. T. Guo wrote the original manuscript, and Y. F. Tang and T. Wei conceived the idea and revised the manuscript.

Data availability

The data supporting this article have been included as part of the ESI.†

Conflicts of interest

There are no conflicts to declare.

Acknowledgements

This work was financially supported by the National Natural Science Foundation of China (No. 21701083, 22179054) and the Key Technologies R & D Program of Jiangsu Province (BZ2023010).

Notes and references

1 M. R. Palacín and A. de Guibert, *Science*, 2016, **351**, 1253292.
2 W. Li, H. Yao, K. Yan, G. Zheng, Z. Liang, Y.-M. Chiang and Y. Cui, *Nat. Commun.*, 2015, **6**, 7436.
3 Y. Lei, Y. Xie, Y. Huang, Q. Wang, Z. Li, X. Wu, Y. Qiao, P. Dai, L. Huang and Y. Hua, *et al.*, *Chem. Commun.*, 2021, **57**, 10055–10058.
4 S. Wang, L. He, M. Wang, X. Guo, X. Qiu, S. Xu, P. Senin, T. Bian and T. Wei, *Particuology*, 2024, **93**, 203–210.
5 J. W. Choi and D. Aurbach, *Nat. Rev. Mater.*, 2016, **1**, 16013.
6 Z. Wang, Z. Du, Y. Liu, C. E. Knapp, Y. Dai, J. Li, W. Zhang, R. Chen, F. Guo, W. Zong, X. Gao, J. Zhu, C. Wei and G. He, *eScience*, 2024, **4**, 100189.

 This journal is © The Royal Society of Chemistry 2025

Published on 30 mis Genver 2025. Downloaded on 19/04/2026 22:10:03.

7 D. Li, S. Zhang, Q. Zhang, P. Kaghazchi, H. Qi, J. Liu, Z. Guo, L. Wang and Y. Wang, *Energy Storage Mater.*, 2020, **26**, 593–603.
8 C. Wang, S. Liu, H. Xu, X. Wang, G. Tian, F. Fan, P. Liu, S. Wang, C. Zeng and C. Shu, *Small*, 2024, **20**, 2308995.
9 C. Wang, T. Ouyang, X. Wang, S. Liu, G. Tian, F. Fan, P. Liu, S. Wang, C. Zeng and C. Shu, *J. Energy Chem.*, 2024, **99**, 384–392.
10 C. Wang, S. Liu, X. Wang, G. Tian, F. Fan, P. Liu, S. Wang, C. Zeng and C. Shu, *Chem. Commun.*, 2024, **60**, 7045–7048.
11 L. Grande, E. Paillard, J. Hassoun, J. B. Park, Y. J. Lee, Y. K. Sun, S. Passerini and B. Scrosati, *Adv. Mater.*, 2015, **27**, 784–800.
12 M. Winter, B. Barnett and K. Xu, *Chem. Rev.*, 2018, **118**, 11433–11456.
13 L. Wang, S. Xu, Z. Song, W. Jiang, S. Zhang, X. Jian and F. Hu, *InfoMat*, 2024, **6**, e12551.
14 H. Zhang, L. Huang, H. Xu, X. Zhang, Z. Chen, C. Gao, C. Lu, Z. Liu, M. Jiang and G. Cui, *eScience*, 2022, **2**, 201–208.
15 Y. Liang, J. Lu, Y. Zhao, R. Chen, X. Guo, M. Wang, S. Wang, Q. Huang, W. Zhao, C. Xu and T. Wei, *Ionics*, 2024, **30**, 709–717.
16 T. Wei, Q. Zhang, S. Wang, M. Wang, Y. Liu, C. Sun, Y. Zhou, Q. Huang, X. Qiu and F. Tian, *Int. J. Miner., Metall. Mater.*, 2023, **30**, 1897–1905.
17 D. Hu, G. Chen, J. Tian, N. Li, L. Chen, Y. Su, T. Song, Y. Lu, D. Cao, S. Chen and F. Wu, *J. Energy Chem.*, 2021, **60**, 104–110.
18 D. Chen, Y. Liu, C. Xia, Y. Han, Q. Sun, X. Wang, W. Chen, X. Jian, W. Lv, J. Ma and W. He, *InfoMat*, 2022, **4**, e12247.
19 H. Xiao, Y. Li, R. Chen, T. Xie, P. Xu, H. Zhu, J. He, W. Zheng and S. Huang, *eScience*, 2023, **3**, 100134.
20 S. Wang, L. He, M. Wang, X. Guo, R. Chen, X. Qiu, S. Kudashev, T. Wei and Q. Wang, *J. Mater. Sci.*, 2024, **59**, 8650–8668.
21 C. Fang, B. Lu, G. Pawar, M. Zhang, D. Cheng, S. Chen, M. Ceja, J.-M. Doux, H. Musrock and M. Cai, *et al.*, *Nat. Energy*, 2021, **6**, 987–994.
22 T. Wei, X. Guo, Y. Zhou, M. Wang, P. Hao, X. Jiang, J. Lu, R. Li, X. Ye and R. Yang, *Next Energy*, 2025, **7**, 100237.
23 K. Lee, S.-H. Kwon, J. Kim, E. Park, I. Kim, H. C. Ahn, A. Coskun and J. W. Choi, *ACS Energy Lett.*, 2024, **9**, 2201–2211.
24 S. Liu, X. Yu, Y. Yan, T. Zeng, X. Wang, G. Tian, C. Wang, S. Wang, Y. Zeng and C. Shu, *Energy Storage Mater.*, 2023, **62**, 102959.
25 T. Liu, J. Wang, Y. Xu, Y. Zhang and Y. Wang, *Nano-Micro Lett.*, 2021, **13**, 170.
26 L. Zheng, F. Guo, T. Kang, J. Yang, Y. Liu, W. Gu, Y. Zhao, H. Lin, Y. Shen, W. Lu and L. Chen, *Nano Res.*, 2020, **13**, 1324–1331.
27 H. Liu, X. B. Cheng, R. Xu, X. Q. Zhang, C. Yan, J. Q. Huang and Q. Zhang, *Adv. Energy Mater.*, 2019, **9**, 1902254.
28 H. Xiao, Y. Li, R. Chen, T. Xie, P. Xu, H. Zhu, J. He, W. Zheng and S. Huang, *eScience*, 2023, **3**, 2667.
29 D. Zhang, Y. Yin, C. Liu and S. Fan, *Chem. Commun.*, 2015, **51**, 322–325.
30 Z. Yu, Q. Yang, W. Xue, J. Shen, J. Zhang, S. Zhu, S. Li and Y. Li, *Nanoscale*, 2023, **15**, 4529–4535.
31 Z. Guo, Q. Zhang, C. Wang, Y. Zhang, S. Dong and G. Cui, *Adv. Funct. Mater.*, 2022, **32**, 2108993.
32 Q. Wang, C. Yang, J. Yang, K. Wu, C. Hu, J. Lu, W. Liu, X. Sun, J. Qiu and H. Zhou, *Adv. Mater.*, 2019, **31**, 1903248.
33 H. Wang, Q. Wang, X. Cao, Y. He, K. Wu, J. Yang, H. Zhou, W. Liu and X. Sun, *Adv. Mater.*, 2020, **32**, 2001259.
34 S. Mao, Q. Wu, F. Ma, Y. Zhao, T. Wu and Y. Lu, *Chem. Commun.*, 2021, **57**, 840–858.
35 Z. Wang, Z. Du, Y. Liu, C. E. Knapp, Y. Dai, J. Li, W. Zhang, R. Chen, F. Guo and W. Zong, *et al.*, *eScience*, 2024, **4**, 100189.
36 J. Cao, Y. Shi, A. Gao, G. Du, M. Dilxat, Y. Zhang, M. Cai, G. Qian, X. Lu and F. Xie, *et al.*, *Nat. Commun.*, 2024, **15**, 1354.
37 C. Wei, Z. Yao, J. Ruan, Z. Song, A. Zhou, Y. Song, D. Wang, J. Jiang, X. Wang and J. Li, *Chin. Chem. Lett.*, 2024, **35**, 109330.
38 S. Li, J. Huang, Y. Cui, S. Liu, Z. Chen, W. Huang, C. Li, R. Liu, R. Fu and D. Wu, *Nat. Nanotechnol.*, 2022, **17**, 613–621.
39 Y. Cheng, X. Ke and Z. Shi, *Acta Metall. Sin.*, 2020, **34**, 354–358.
40 J. Pokharel, A. Cresce, B. Pant, M. Y. Yang, A. Gurung, W. He, A. Baniya, B. S. Lamsal, Z. Yang and S. Gent, *et al.*, *Nat. Commun.*, 2024, **15**, 3085.
41 H. Kitaura, E. Hosono and H. Zhou, *Energy Environ. Sci.*, 2021, **14**, 4474–4480.
42 Z. Peng, N. Zhao, Z. Zhang, H. Wan, H. Lin, M. Liu, C. Shen, H. He, X. Guo, J.-G. Zhang and D. Wang, *Nano Energy*, 2017, **39**, 662–672.
43 W. Tang, X. Yin, S. Kang, Z. Chen, B. Tian, S. L. Teo, X. Wang, X. Chi, K. P. Loh, H. W. Lee and G. W. Zheng, *Adv. Mater.*, 2018, **30**, 1801745.
44 R. Xu, F. Liu, Y. Ye, H. Chen, R. R. Yang, Y. Ma, W. Huang, J. Wan and Y. Cui, *Adv. Mater.*, 2021, **33**, e2104009.
45 J. Zhang, J. Zhu, R. Zhao, J. Liu, X. Song, N. Xu, Y. Liu, H. Zhang, X. Wan and Y. Ma, *et al.*, *Energy Environ. Sci.*, 2024, **17**, 7119–7128.
46 T. Wei, Z. H. Zhang, Q. Zhang, J. H. Lu, Q. M. Xiong, F. Y. Wang, X. P. Zhou, W. J. Zhao and X. Y. Qiu, *Int. J. Miner., Metall. Mater.*, 2021, **28**, 1636–1646.
47 Q. Zhang, T. Wei, J. Lu, C. Sun, Y. Zhou, M. Wang, Y. Liu, B. Xiao, X. Qiu and S. Xu, *J. Electroanal. Chem.*, 2022, **926**, 116935.
48 P. Qing, Z. Wu, A. Wang, S. Huang, K. Long, T. Naren, D. Chen, P. He, H. Huang and Y. Chen, *et al.*, *Adv. Mater.*, 2023, **35**, e2211203.
49 Z. Yan, J. Liu, Y. Lin, Z. Deng, X. He, J. Ren, P. He, C. Pang, C. Xiao and D. Yang, *et al.*, *Electrochim. Acta*, 2021, **390**, 138814.
50 K. Wu, B. Zhao, C. Yang, Q. Wang, W. Liu and H. Zhou, *J. Energy Chem.*, 2020, **43**, 16–23.
51 T. Li, H. Zhou, W. Liu, J. Gao, Z. Guo, Z. Su, Y. Yan, S. Su, H. Xie, G. Peng and M. Qu, *Chemistry*, 2023, **29**, e202301991.
52 P. Bai, J. Li, F. R. Brushett and M. Z. Bazant, *Energy Environ. Sci.*, 2016, **9**, 3221–3229.
53 Y. Zhang, F. M. Heim, J. L. Bartlett, N. Song, D. Isheim and X. Li, *Sci. Adv.*, 2019, **5**, eaav5577.
54 J. Zheng, M. H. Engelhard, D. Mei, S. Jiao, B. J. Polzin, J.-G. Zhang and W. Xu, *Nat. Energy*, 2017, **2**, 17012.
55 R. Weber, M. Genovese, A. J. Louli, S. Hames, C. Martin, I. G. Hill and J. R. Dahn, *Nat. Energy*, 2019, **4**, 683–689.
56 J. I. Yamaki, S. I. Tobishima, K. Hayashi, K. Saito, Y. Nemoto and M. Arakawa, *J. Power Sources*, 1998, **74**, 219–227.
57 F. Shi, A. Pei, A. Vailionis, J. Xie, B. Liu, J. Zhao, Y. Gong and Y. Cui, *Proc. Natl. Acad. Sci. U. S. A.*, 2017, **114**, 12138–12143.
58 A. Pei, G. Zheng, F. Shi, Y. Li and Y. Cui, *Nano Lett.*, 2017, **17**, 1132–1139.
59 B. Liu, J.-G. Zhang and W. Xu, *Joule*, 2018, **2**, 833–845.
60 Y. Liu, D. Lin, Y. Li, G. Chen, A. Pei, O. Nix, Y. Li and Y. Cui, *Nat. Commun.*, 2018, **9**, 3656.
61 X. B. Cheng, R. Zhang, C. Z. Zhao and Q. Zhang, *Chem. Rev.*, 2017, **117**, 10403–10473.
62 62Y. Wang, Z. Wang, D. Lei, W. Lv, Q. Zhao, B. Ni, Y. Liu, B. Li, F. Kang and Y. B. He, *ACS Appl. Mater. Interfaces*, 2018, **10**, 20244–20249.
63 Q. He, Z. Li, M. Wu, M. Xie, F. Bu, H. Zhang, R. Yu, L. Mai and Y. Zhao, *Adv. Mater.*, 2023, **35**, 2302418.
64 C. Wang, C. Yang, Y. Du, Z. Guo and H. Ye, *Adv. Funct. Mater.*, 2023, **33**, 2303427.
65 S. Chandrashekar, N. M. Trease, H. J. Chang, L. S. Du, C. P. Grey and A. Jerschow, *Nat. Mater.*, 2012, **11**, 311–315.
66 G. Li, *Adv. Energy Mater.*, 2021, **11**, 2002891.
67 W. Ren, Y. Zheng, Z. Cui, Y. Tao, B. Li and W. Wang, *Energy Storage Mater.*, 2021, **35**, 157–168.
68 J. Zheng, P. Yan, D. Mei, M. H. Engelhard, S. S. Cartmell, B. J. Polzin, C. Wang, J.-G. Zhang and W. Xu, *Adv. Energy Mater.*, 2016, **6**, 1502151.
69 S. Rajendran, Z. Tang, A. George, A. Cannon, C. Neumann, A. Sawas, E. Ryan, A. Turchanin and L. M. R. Arava, *Adv. Energy Mater.*, 2021, **11**, 2100666.
70 H. J. S. Sand, *Proc. Phys. Soc. Lond.*, 1899, **17**, 496.
71 C. Brissot, M. Rosso, J. N. Chazalviel and S. Lascaud, *J. Power Sources*, 1999, **81–82**, 925–929.
72 J. N. Chazalviel, *Phys. Rev. A:At., Mol., Opt. Phys.*, 1990, **42**, 7355–7367.
73 X. Chen, X. R. Chen, T. Z. Hou, B. Q. Li, X. B. Cheng, R. Zhang and Q. Zhang, *Sci. Adv.*, 2019, **5**, eaau7728.
74 Y. Yan, C. Shu, R. Zheng, M. Li, Z. Ran, M. He, A. Hu, T. Zeng, H. Xu and Y. Zeng, *Nano Res.*, 2022, **15**, 3150–3160.
75 J. Chazalviel, *Phys. Rev. A: At., Mol., Opt. Phys.*, 1990, **42**, 7355–7367.
76 V. Fleury, J. N. Chazalviel, M. Rosso and B. Sapoval, *J. Electroanal. Chem. Interfacial Electrochem.*, 1990, **290**, 249–255.
77 M. D. Tikekar, S. Choudhury, Z. Tu and L. A. Archer, *Nat. Energy*, 2016, **1**, 16114.
78 Q. Yun, Y.-B. He, W. Lv, Y. Zhao, B. Li, F. Kang and Q.-H. Yang, *Adv. Mater.*, 2016, **28**, 6932–6939.
79 C.-P. Yang, Y.-X. Yin, S.-F. Zhang, N.-W. Li and Y.-G. Guo, *Nat. Commun.*, 2015, **6**, 8058.
80 X. R. Chen, B. C. Zhao, C. Yan and Q. Zhang, *Adv. Mater.*, 2021, **33**, e2004128.
81 B. Thirumalraj, T. T. Hagos, C. J. Huang, M. A. Teshager, J. H. Cheng, W. N. Su and B. J. Hwang, *J. Am. Chem. Soc.*, 2019, **141**, 18612–18623.

Published on 30 mis Genver 2025. Downloaded on 19/04/2026 22:10:03.

82 D. R. Ely and R. E. García, *J. Electrochem. Soc.*, 2013, **160**, A662.
83 X. Shen, S. Shi, B. Li, S. Li, H. Zhang, S. Chen, H. Deng, Q. Zhang, J. Zhu and X. Duan, *Adv. Funct. Mater.*, 2022, **32**, 2206388.
84 Y. Yao, J. Wan, N.-Y. Liang, Y. Chong, R. Wen and Q. Zhang, *J. Am. Chem. Soc.*, 2023, **145**, 8001–8006.
85 J. A. Sethian and J. Straint, *J. Comput. Phys.*, 1992, **98**, 231–253.
86 J. Steiger, G. Richter, M. Wenk, D. Kramer and R. Mönig, *Electrochem. Commun.*, 2015, **50**, 11–14.
87 J. Steiger, D. Kramer and R. Mönig, *J. Power Sources*, 2014, **261**, 112–119.
88 P. Zou, Y. Sui, H. Zhan, C. Wang, H. L. Xin, H.-M. Cheng, F. Kang and C. Yang, *Chem. Rev.*, 2021, **121**, 5986–6056.
89 E. Kazyak, K. N. Wood and N. P. Dasgupta, *Chem. Mater.*, 2015, **27**, 6457–6462.
90 Z. Tu, S. Choudhury, M. J. Zachman, S. Wei, K. Zhang, L. F. Kourkoutis and L. A. Archer, *Nat. Energy*, 2018, **3**, 310–316.
91 V. Yurkiv, T. Foroozan, A. Ramasubramanian, R. Shahbazian-Yassar and F. Mashayek, *Electrochim. Acta*, 2018, **265**, 609–619.
92 J. Steiger, D. Kramer and R. Mönig, *Electrochim. Acta*, 2014, **136**, 529–536.
93 A. Pei, G. Zheng, F. Shi, Y. Li and Y. Cui, *Nano Lett.*, 2017, **17**, 1132–1139.
94 F. Orsini, A. du Pasquier, B. Beaudouin, J. M. Tarascon, M. Trentin, N. Langenhuizen, E. de Beer and P. Notten, *J. Power Sources*, 1999, **81–82**, 918–921.
95 H. Jing, H. Xing, B. Li and Y. Han, *Energy Mater. Adv.*, 2023, **4**, 0018.
96 H. Ye, S. Xin, Y.-X. Yin, J.-Y. Li, Y.-G. Guo and L.-J. Wan, *J. Am. Chem. Soc.*, 2017, **139**, 5916–5922.
97 Z. Wang, C. Sun, Y. Shi, F. Qi, Q. Wei, X. Li, Z. Sun, B. An and F. Li, *J. Power Sources*, 2019, **439**, 227073.
98 M. Zhu, K. Xu, D. Li, T. Xu, W. Sun, Y. Zhu and Y. Qian, *ACS Appl. Mater. Interfaces*, 2020, **12**, 38098–38105.
99 T.-S. Wang, X. Liu, X. Zhao, P. He, C.-W. Nan and L.-Z. Fan, *Adv. Funct. Mater.*, 2020, **30**, 2000786.
100 Y. Shi, G.-X. Liu, J. Wan, R. Wen and L.-J. Wan, *Sci. China Chem.*, 2021, **64**, 734–738.
101 Q.-Y. Yang, Z. Yu, Y. Li, W. Zhang, H.-W. Yuan, H.-J. Li, W. Ma, S.-M. Zhu and S. Li, *Rare Met.*, 2022, **41**, 2800–2818.
102 Y. Zhao, L. Li, D. Zhou, Y. Shan, X. Chen and W. Cui, *Energy Environ. Mater.*, 2023, **6**, e12463.
103 M. Han, G. Liu, J. Jiang, S. Lu, Y. Jiang, Y. Liu, B. Zhao and J. Zhang, *ACS Appl. Mater. Interfaces*, 2021, **13**, 48828–48837.
104 J. Park, J. I. Jung, S. Ha, D. H. Kim, H.-S. Jang, B. H. Kim, H.-K. Lim, H.-J. Jin and Y. S. Yun, *Angew. Chem., Int. Ed.*, 2024, **63**, e202409992.
105 C. Wang, H. Wang, L. Tao, X. Wang, P. Cao, F. Lin and H. L. Xin, *ACS Energy Lett.*, 2023, **8**, 1929–1935.
106 M. Tao, X. Chen, H. Lin, Y. Jin, P. Shan, D. Zhao, M. Gao, Z. Liang and Y. Yang, *ACS Nano*, 2023, **17**, 24104–24114.
107 A. Jana, D. R. Ely and R. E. García, *J. Power Sources*, 2015, **275**, 912–921.
108 J. Sun, J. Peng, T. Ring, L. Whittaker-Brooks, J. Zhu, D. Fraggedakis, J. Niu, T. Gao and F. Wang, *Energy Environ. Sci.*, 2022, **15**, 5284–5299.
109 Y. Xu, H. Wu, Y. He, Q. Chen, J.-G. Zhang, W. Xu and C. Wang, *Nano Lett.*, 2020, **20**, 418–425.
110 A. C. Thenuwara, P. P. Shetty, N. Kondekar, S. E. Sandoval, K. Cavallaro, R. May, C.-T. Yang, L. E. Marbella, Y. Qi and M. T. McDowell, *ACS Energy Lett.*, 2020, **5**, 2411–2420.
111 W. Fang, Z. Wen, L. Chen, Z. Qin, J. Li, Z. Zheng, Z. Weng, G. Wu, N. Zhang and X. Liu, *et al.*, *Nano Energy*, 2022, **104**, 107881.
112 F. Shi, A. Pei, A. Vailionis, J. Xie, B. Liu, J. Zhao, Y. Gong and Y. Cui, *Proc. Natl. Acad. Sci. U. S. A.*, 2017, **114**, 12138–12143.
113 J. Lu, L. Li, J.-B. Park, Y.-K. Sun, F. Wu and K. Amine, *Chem. Rev.*, 2014, **114**, 5611–5640.
114 J. Liu, S. Ihuaenyi, R. Kuphal, J. Salinas, L. Xie, L. Yang, U. Janakiraman, M. E. Fortier and C. Fang, *J. Electrochem. Soc.*, 2023, **170**, 010535.
115 D. Aurbach, O. Youngman, Y. Gofer and A. Meitav, *Electrochim. Acta*, 1990, **35**, 625–638.
116 K. Xu, *Chem. Rev.*, 2004, **104**, 4303–4418.
117 Y.-K. Sun, S.-T. Myung, B.-C. Park, J. Prakash, I. Belharouak and K. Amine, *Nat. Mater.*, 2009, **8**, 320–324.
118 J. Qian, W. A. Henderson, W. Xu, P. Bhattacharya, M. Engelhard, O. Borodin and J.-G. Zhang, *Nat. Commun.*, 2015, **6**, 6362.
119 L. Suo, W. Xue, M. Gobet, S. G. Greenbaum, C. Wang, Y. Chen, W. Yang, Y. Li and J. Li, *Proc. Natl. Acad. Sci. U. S. A.*, 2018, **115**, 1156–1161.
120 C. Yan, Y.-X. Yao, X. Chen, X.-B. Cheng, X.-Q. Zhang, J.-Q. Huang and Q. Zhang, *Angew. Chem., Int. Ed.*, 2018, **57**, 14055–14059.
121 Z. Jin, Y. Liu, H. Xu, T. Chen and C. Wang, *Angew. Chem., Int. Ed.*, 2024, **63**, e202318197.
122 Y. Liang, W. Wu, D. Li, H. Wu, C. Gao, Z. Chen, L. Ci and J. Zhang, *Adv. Energy Mater.*, 2022, **12**, 2202493.
123 S. Liu, J. Xia, W. Zhang, H. Wan, J. Zhang, J. Xu, J. Rao, T. Deng, S. Hou, B. Nan and C. Wang, *Angew. Chem., Int. Ed.*, 2022, **61**, e202210522.
124 F. Wang, Z. Wen, Z. Zheng, W. Fang, L. Chen, F. Chen, N. Zhang, X. Liu, R. Ma and G. Chen, *Adv. Energy Mater.*, 2023, **13**, 2203830.
125 Y. Luo, T. Li, X. Yang, H. Zhang, Z. Jia, J. Yan and X. Li, *Adv. Energy Mater.*, 2022, **12**, 2103503.
126 S. H. Park and Y. J. Lee, *J. Mater. Chem. A*, 2021, **9**, 1803–1811.
127 K. Dong, Y. Xu, J. Tan, M. Osenberg, F. Sun, Z. Kochovski, D. T. Pham, S. Mei, A. Hilger and E. Ryan, *et al.*, *ACS Energy Lett.*, 2021, **6**, 1719–1728.
128 X.-R. Chen, Y.-X. Yao, C. Yan, R. Zhang, X.-B. Cheng and Q. Zhang, *Angew. Chem., Int. Ed.*, 2020, **59**, 7743–7747.
129 S. Jo, B. Kwon, J. Oh, J. Lee, K. Park and K. T. Lee, *J. Mater. Chem. A*, 2022, **10**, 5520–5529.
130 G. Jiang, N. Jiang, N. Zheng, X. Chen, J. Mao, G. Ding, Y. Li, F. Sun and Y. Li, *Energy Storage Mater.*, 2019, **23**, 181–189.
131 Q. Li, J. Zhang, Y. Zeng, Z. Tang, D. Sun, Z. Peng, Y. Tang and H. Wang, *Chem. Commun.*, 2022, **58**, 2597–2611.
132 C. P. Yang, Y. X. Yin, S. F. Zhang, N. W. Li and Y. G. Guo, *Nat. Commun.*, 2015, **6**, 8058.
133 H. Liu, X. Yue, X. Xing, Q. Yan, J. Huang, V. Petrova, H. Zhou and P. Liu, *Energy Storage Mater.*, 2019, **16**, 505–511.
134 W. Jia, J. Zhang, L. Zheng, H. Zhou, W. Zou and L. Wang, *eScience*, 2024, **4**, 100266.
135 Y. Liu, D. Lin, Z. Liang, J. Zhao, K. Yan and Y. Cui, *Nat. Commun.*, 2016, **7**, 10992.
136 D. Lin, Y. Liu, Z. Liang, H. W. Lee, J. Sun, H. Wang, K. Yan, J. Xie and Y. Cui, *Nat. Nanotechnol.*, 2016, **11**, 626–632.
137 Z. Liang, D. Lin, J. Zhao, Z. Lu, Y. Liu, C. Liu, Y. Lu, H. Wang, K. Yan, X. Tao and Y. Cui, *Proc. Natl. Acad. Sci. U. S. A.*, 2016, **113**, 2862–2867.
138 S. S. Chi, Y. Liu, W. L. Song, L. Z. Fan and Q. Zhang, *Adv. Funct. Mater.*, 2017, **27**, 1700348.
139 S. Huang, H. Yang, J. Hu, Y. Liu, K. Wang, H. Peng, H. Zhang and L. Z. Fan, *Small*, 2019, **15**, e1904216.
140 C. Yan, X. B. Cheng, Y. Tian, X. Chen, X. Q. Zhang, W. J. Li, J. Q. Huang and Q. Zhang, *Adv. Mater.*, 2018, **30**, e1707629.
141 T. Wei, M. Wang, Y. Zhou, X. Guo, S. Wang, Y. Liu, C. Sun and Q. Wang, *Chin. J. Chem. Eng.*, 2024, **71**, 13–23.
142 Y. Liu, X. Guo, Y. Zhou, M. Wang, C. Sun, S. Xu, X. Qiu, Q. Huang and T. Wei, *CrystEngComm*, 2024, **26**, 681–690.
143 T. Wei, Y. Zhou, C. Sun, L. Liu, S. Wang, M. Wang, Y. Liu, Q. Huang, Q. Zhuang and Y. Tang, *Particuology*, 2024, **84**, 89–97.
144 X. Hao, Q. Zhao, S. Su, S. Zhang, J. Ma, L. Shen, Q. Yu, L. Zhao, Y. Liu, F. Kang and Y. B. He, *Adv. Energy Mater.*, 2019, **9**, 1901604.
145 Z. Huang, G. Zhou, W. Lv, Y. Deng, Y. Zhang, C. Zhang, F. Kang and Q.-H. Yang, *Nano Energy*, 2019, **61**, 47–53.
146 M. Cai, Y. Lu, L. Yao, J. Jin and Z. Wen, *Chem. Eng. J.*, 2021, **417**, 129158.
147 T. Deng, X. Ji, Y. Zhao, L. Cao, S. Li, S. Hwang, C. Luo, P. Wang, H. Jia and X. Fan, *et al.*, *Adv. Mater.*, 2020, **32**, e2000030.
148 F. Zhao, X. Zhou, W. Deng and Z. Liu, *Nano Energy*, 2019, **62**, 55–63.
149 T. Wei, J. Lu, M. Wang, C. Sun, Q. Zhang, S. Wang, Y. Zhou, D. Chen and Y. Q. Lan, *Chin. J. Chem.*, 2023, **41**, 1861–1874.
150 T. Wei, J. Lu, P. Zhang, G. Yang, C. Sun, Y. Zhou, Q. Zhuang and Y. Tang, *Chin. Chem. Lett.*, 2023, **34**, 107947.
151 Z. Zhuang, F. Zhang, D. Gandla, V. V. Jadhav, Z. Liu, L. Hu, F. Lu and D. Q. Tan, *ACS Appl. Mater. Interfaces*, 2023, **15**, 38530–38539.
152 T. Wei, C. Sun, X. Guo, Y. Zhou, M. Wang, X. Qiu, Q. Wang and Y. Tang, *J. Colloid Interface Sci.*, 2024, **664**, 596–606.
153 M. Wang, T. Wei, J. Lu, X. Guo, C. Sun, Y. Zhou, C. Su, S. Chen, Q. Wang and R. Yang, *ChemSusChem*, 2024, **17**, e202400569.
154 C. Sun, J. Lu, X. Guo, Y. Zhou, M. Wang, X. Qiu, Q. Wang, R. Yang and T. Wei, *J. Power Sources*, 2024, **607**, 234597.
155 G. Huang, P. Guo, J. Wang, S. Chen, J. Liang, R. Tao, S. Tang, X. Zhang, S. Cheng, Y.-C. Cao and S. Dai, *Chem. Eng. J.*, 2020, **384**, 123313.
156 J. Sun, Y. Cheng, H. Zhang, X. Yan, Z. Sun, W. Ye, W. Li, M. Zhang, H. Gao and J. Han, *et al.*, *Nano Lett.*, 2022, **22**, 5874–5882.

 This journal is © The Royal Society of Chemistry 2025

157 Z. Zhuang, C. Liu, Y. Yan, P. Ma and D. Q. Tan, *J. Mater. Chem. A*, 2021, **9**, 27095–27101.
158 J. Yun, B.-K. Park, E.-S. Won, S. H. Choi, H. C. Kang, J. H. Kim, M.-S. Park and J.-W. Lee, *ACS Energy Lett.*, 2020, **5**, 3108–3114.
159 Y. Zhao, L. Wang, J. Zou, Q. Ran, L. Li, P. Chen, H. Yu, J. Gao and X. Niu, *J. Energy Chem.*, 2022, **65**, 666–673.
160 J. Pu, J. Li, K. Zhang, T. Zhang, C. Li, H. Ma, J. Zhu, P. V. Braun, J. Lu and H. Zhang, *Nat. Commun.*, 2019, **10**, 1896.
161 K. H. Park, D. W. Kang, J.-W. Park, J.-H. Choi, S.-J. Hong, S. H. Song, S.-M. Lee, J. Moon and B. G. Kim, *J. Mater. Chem. A*, 2021, **9**, 1822–1834.
162 T. Li, S. Gu, L. Chen, L. Zhang, X. Qin, Z. Huang, Y. B. He, W. Lv and F. Kang, *Small*, 2022, **18**, e2203273.
163 T. Wei, J. Lu, P. Zhang, Q. Zhang, G. Yang, R. Yang, D. Chen, Q. Wang and Y. Tang, *Chin. Chem. Lett.*, 2024, **35**, 109122.
164 T. Wei, Y. Zhou, C. Sun, X. Guo, S. Xu, D. Chen and Y. Tang, *Nano Res.*, 2023, **17**, 2763–2769.

Published on 30 mis Genver 2025. Downloaded on 19/04/2026 22:10:03.